

1 **Mesozoic–Cenozoic multistage tectonic evolution of the Pamir: detrital fission-**
2 **track constraints from the Tajik Basin**

3 **Lin Li^{1,2*}, Yani Najman³, Guillaume Dupont-Nivet^{1,4}, Mauricio Parra⁵, Pierrick Roperch¹,**
4 **Mustafa Kaya⁶, Niels Meijer⁷, Paul O’Sullivan⁸, Gilby Jepson², Jovid Aminov⁹**

5 ¹Géosciences Rennes-UMR 6118, CNRS-University of Rennes, Rennes, France

6 ²Department of Geosciences, University of Arizona, Tucson, USA

7 ³Lancaster Environment Centre, Lancaster University, Lancaster, UK

8 ⁴Institute of Geosciences, Potsdam University, Potsdam, Germany

9 ⁵Institute of Energy and Environment, University of São Paulo, São Paulo, Brazil

10 ⁶Department of Geological Engineering, Middle East Technical University, Ankara, Türkiye

11 ⁷Senckenberg Biodiversity and Climate Research Center (SBIK-F), Frankfurt, Germany

12 ⁸GeoSeps Services, Moscow, Idaho, USA

13 ⁹Institute of geology, earthquake engineering and seismology, Academy of Sciences, Dushanbe,
14 Republic of Tajikistan

15 *Corresponding author email: li.lin8611@gmail.com; linli2@arizona.edu

16

17 **Highlights:**

- 18 • Pamir exhumation is interpreted from vitrinite reflectance, fission-track and U-Pb dating of
19 Tajik Basin strata
- 20 • The Cimmerian orogeny (Late Triassic–Early Jurassic) and Neo-Tethyan subduction (mid-
21 Cretaceous) were recorded
- 22 • Further exhumation during the Late Eocene–Neogene is associated with the Pamir’s ongoing
23 formation

24 **Abstract**

25 Knowledge of the tectonic history of the Pamir contributes to our understanding of both the
26 evolution of collisional orogenic belts as well as factors controlling Central Asian aridification. It
27 is, however, not easy to decipher the Mesozoic–Cenozoic tectonics of the Pamir due to extensive
28 Neogene deformation in an orogen that remains largely understudied. This study reports detrital
29 apatite and zircon fission-track (FT) ages from both the eastern Tajik Basin sedimentary rocks and
30 Pamir modern river sands. These FT data, supported by vitrinite reflectance and zircon and apatite
31 U-Pb double dating, suggest that the majority of the FT ages are unreset and record exhumation
32 stages of the Pamir, which has served as the source terrane of the Tajik Basin since the Cretaceous.
33 Further, we combine the new data with a compilation of published detrital apatite and zircon FT
34 data from both the Tajik Basin sedimentary rocks and Pamir modern river sands, to explore the
35 Mesozoic–Cenozoic tectonic history of Pamir. Deconvolved FT Peak Ages document two major
36 Mesozoic exhumation events associated with the Late Triassic–Early Jurassic Cimmerian orogeny
37 that reflects accretion of the Pamir terranes, as well as the Early–early Late Cretaceous deformation
38 associated with the northward subduction of the Neo-Tethys Ocean beneath Pamir. The compiled
39 data also show significant Late Eocene–Neogene exhumation associated with the ongoing
40 formation of the Pamir, which peaks at ~36 Ma, ~25 Ma, ~14 Ma, and ~7 Ma.

41

42 **Keywords:** Tajik Basin; Detrital fission-track; Double dating; Pamir tectonics; Mesozoic–
43 Cenozoic; Exhumation

44

45 **1. Introduction**

46 Knowledge of Pamir evolution is important not only for understanding crustal deformation
47 processes (Burtman and Molnar, 1993; Robinson, 2015; Rutte et al., 2017a; Sobel et al., 2013),
48 but also for elucidating the impact of such processes on regional climate changes (Heermance et
49 al., 2018; Wang et al., 2020). Significant advances have been made over the last two decades, both
50 with regard to the deep structure (e.g., Kufner et al., 2021; Kufner et al., 2016; Schmidt et al., 2011;
51 Schneider et al., 2013; Schwab et al., 2004; Sippl et al., 2013) and the geological evolution of the
52 orogen (e.g., Robinson et al., 2004; Searle and Hacker, 2018; Stearns et al., 2013). However, major
53 first-order questions remain unresolved to establish relationships between deep and surface
54 processes and to understand the role of inherited Mesozoic structures on the Cenozoic Pamir
55 evolution.

56 The Pamir consists of the North, Central, South Pamir, and Karakoram terranes (Fig 1). The
57 latter three terranes are interpreted as fragments of Gondwana that drifted across the Tethys Ocean
58 during the Mesozoic, subsequently docking with the southern margin of Asia, i.e., North Pamir
59 (Angiolini et al., 2013; Robinson, 2015). Existing studies infer near synchronous closure of the
60 Paleo-Tethys oceans which previously separated the different terranes of the Pamir, during the
61 latest Triassic–Early Jurassic Cimmerian orogeny (Angiolini et al., 2013; Robinson, 2015). A
62 phase of Mid-Cretaceous contractional deformation has also been inferred for the North and South
63 Pamir, which was attributed to the northward subduction of the Neo-Tethys Ocean beneath the
64 Pamir (Chapman et al., 2018a; Robinson, 2015). This inference is largely derived from
65 explorations in the northeastern and southeastern Pamir. Other parts of the Pamir, especially the
66 Central and western Pamir, may not share a similar Mid-Cretaceous tectonic history. For example,
67 it has been inferred that the Central Pamir was at sea level during the Late Cretaceous (He et al.,

68 2018; Zhang et al., 2019). Documenting the existence and extent of these Mesozoic events and
69 their ages is important to better understand the subsequent Cenozoic evolution. Detrital records
70 provide unique opportunities to explore the tectonic history of source terranes for large areas.

71 Multiple deformation and exhumation stages have been proposed for the Cenozoic evolution
72 of the Pamir. Based on low-temperature thermochronological data of bedrock in the northeastern
73 Pamir, Amidon and Hynek (2010) identified two punctuated accelerated exhumation phases at 50–
74 40 Ma and 25–16 Ma, respectively. Similarly, Sobel et al. (2013) proposed initiation of Cenozoic
75 deformation and northward translation of the Pamir since ~25 Ma. Structural and
76 thermochronological studies in the Central Pamir indicate intense contractional deformation
77 during the Late Eocene and Late Oligocene (~35–22 Ma), followed by Early–Middle Miocene
78 (20–12 Ma) exhumation of gneiss domes (Rutte et al., 2017a; Rutte et al., 2017b). Based on the
79 observation of synchronous wetting and drying in the Tajik and Tarim basins, respectively, Wang
80 et al. (2020) inferred that the Pamir probably reached significant elevations around 25 Ma.
81 Furthermore, based on synchronous shifts of provenance and stable isotopes, Li et al. (2022)
82 inferred a phase of deformation and surface uplift in the North Pamir since ~12 Ma, in line with
83 coeval initiation of aeolian deposits in the Tarim Basin interpreted to reflect the closure of the wind
84 gap between the Pamir and Tian Shan (Heermance et al., 2018). This study aims to further
85 elucidate the protracted history of the formation of the Pamir by identifying and dating
86 exhumation events using low-temperature thermochronology on detrital records of the orogen.

87 Apatite and zircon fission-track dating record the cooling of the upper few kilometers (e.g.,
88 3–10 km) of crust, and thus reflect its exhumation history (Gallagher et al., 1998). Unlike bedrock
89 fission-track methods, which commonly record the most recent exhumation, detrital fission-track
90 ages from stratigraphic successions record the evolving exhumation history of eroded rock units

91 in the hinterland, and thus may provide a much longer record of the source terrane exhumation
92 (Garver et al., 1999; Ruiz et al., 2004). This study reports both detrital apatite and detrital zircon
93 fission-track ages from a composite early Late Cretaceous–Late Miocene sedimentary section in
94 the eastern Tajik Basin that has been recently dated using magnetostratigraphy (Kaya et al., 2020;
95 Li et al., 2022), and from modern river sands from the western Pamir to complement existing
96 source characterizations. Both fission-track and U-Pb methods were used to double date single
97 grains in order to better evaluate exhumation signals. Vitrinite reflectance data was gathered to
98 estimate burial temperature and assess potential resetting of the fission-track signal. Combined
99 with published detrital fission-track data from both modern river sands from the Pamir and
100 sedimentary rocks of the Tajik Basin, this study explores the Mesozoic–Cenozoic exhumation
101 history of the Pamir.

102

103 **2. Geologic background**

104 **2.1. Pamir**

105 The Pamir-Karakoram is separated from the Alai Basin and Southwest Tian Shan by the
106 Main Pamir thrust to the north, from the Tarim Basin by the Kashgar-Yecheng transfer system to
107 the east, from the Tajik Basin by the Darvaz fault to the west, and from the Kohistan-Ladakh arc
108 by the Shyok suture to the south (Fig. 1A). In the southeast and southwest, the Pamir connects to
109 the Tibetan Plateau and the Hindu Kush, respectively (Fig. 1A). The North Pamir, Central Pamir,
110 South Pamir, and Karakoram terranes are separated by the Tanymas suture, Rushan-Pshart suture,
111 and Tirich-Mir boundary zone (TBZ) (Fig. 1A), respectively. The North Pamir can be further
112 divided into the Oytog, Darvaz, and Karakul-Mazar terranes (Fig. 1A) (Rembe et al., 2021;
113 Robinson et al., 2012; Schwab et al., 2004).

114 The Central Pamir, South Pamir, and Karakoram are all Gondwana-affiliated terranes, that
115 drifted northward as one block toward the Eurasian continent during the Carboniferous–Permian
116 (Angiolini et al., 2013; Robinson, 2015). During the Late Permian–Middle Triassic, rifting
117 occurred between the Central and South Pamir, as well as between the South Pamir and Karakoram
118 to create the Rushan Ocean and TBZ Basin (Angiolini et al., 2013; Robinson, 2015), both of which
119 may represent narrow and never fully developed oceanic spreading centers (Leven, 1995; Zanchi
120 and Gaetani, 2011). During the same period, the Paleo-Tethys ocean between the North and
121 Central Pamir began to subduct northward to form the Karakul-Mazar magmatic complex (Schwab
122 et al., 2004). The post-Middle Triassic tectonic evolution of the Pamir will be discussed in more
123 detail later in this paper (e.g., section 6).

124 The modern Pamir is largely drained by the West-flowing Panj River into the Tajik Basin,
125 and the tributaries of the Panj River drain the South, Central, and North Pamir (Fig. 1A). In contrast,
126 only the easternmost part of the Pamir is drained by rivers into the Tarim Basin (Fig 1A). Due to
127 this asymmetrical modern drainage configuration, and the argument that this asymmetrical
128 configuration has existed at least since the Early Miocene (Carrapa et al., 2014), or even since the
129 late Eocene (Jia et al., 2021), the Tajik Basin detritus, compared to detritus from the Tarim Basin,
130 is more likely to record a comprehensive exhumation and tectonic history of the Pamir.

131

132 **2.2. The Tajik Basin**

133 The Tajik Basin is bounded by mountain belts on all sides, except its southwest corner: the
134 Pamir to the east, the southwest Tian Shan to the north (Tajik Gissar) and northwest (Uzbek Gissar),
135 and the Hindu Kush to the south (Fig. 1A). The Tajik Basin has probably been a foreland basin of
136 the Pamir hinterland since the late Early Cretaceous (Chapman et al., 2020), or even since the late

137 Jurassic (Kaya et al., 2020); and thus has received detritus mainly shed from the different terranes
138 of the Pamir during the Cretaceous and Cenozoic.

139 Internally, the Tajik Basin is characterized by north–south trending fold-thrust belts, which
140 run parallel to the front of the Pamir hinterland, i.e., the Darvaz fault (Fig. 1A) (Chapman et al.,
141 2017; Gaḡała et al., 2020). Shortening estimates of the fold-thrust belt vary significantly from ~65–
142 70 km (Chapman et al., 2017), to ~93–148 km (Gaḡała et al., 2020), to ~240 km (Bourgeois et al.,
143 1997). Low-temperature thermochronology studies yield relatively well-constrained ages for the
144 initiation of the fold-thrust belt since ~16–12 Ma (Abdulhameed et al., 2020; Chapman et al., 2017).
145 In addition to east–west shortening, the detached fold-thrust belts in the Tajik Basin also
146 experienced counterclockwise rotations that decrease from the eastern basin (~60°) to the western
147 basin (~0°) (Bazhenov et al., 1994; Pozzi and Feinberg, 1991; Thomas et al., 1994). The timing of
148 the rotation, however, remains controversial due to poor age constraints in the basin (Bosboom et
149 al., 2014; Thomas et al., 1994; Zhang and Sun, 2020).

150

151 **2.3. Studied sections and age constraints**

152 We collected detrital samples from a >4400 m long composite sedimentary section in the
153 eastern Tajik Basin (Fig. 1B): the Khirmanjo (KH) and Shurobod (SB) sections, which were
154 recently measured and dated in Kaya et al. (2020) and Li et al. (2022). These two sections cover a
155 long succession from the late Early Cretaceous to the Late Miocene (Fig. 2). The lower ~700 m of
156 the section is dominated by alluvial plain sandstones, with several intervals of coastal plain and
157 tidal deposits of mudstones and sandstones (Kaya et al., 2020). Between 700 m and 1400 m, the
158 rocks are dominated by marine tidal and carbonate ramp deposits, with intervals of coastal plain
159 deposits (Kaya et al., 2020). The 1400–1600 m interval is a condensed section covering several

160 marine transgression and regression cycles. From 1600 m to the top of the section, the rocks are
161 all terrestrial red-colored clastic rocks (Li et al., 2022): the 1600–2600 m interval is classified as
162 the Baldshuan Formation, which includes three members: the fine-grained Shurisay Member
163 (1600–1800 m), the conglomerate-dominated Kamolin Member (1800–1950 m), and the fine-
164 grained Childara Member with numerous conglomerate interlayers (1950–2600 m); the Chingou
165 Formation at the top of the section is dominated by conglomerates with mudstone intervals. Both
166 the Baldshuan and Chingou formations are dominated by braided river deposits, with a small part
167 of the Chingou Formation characterized by alluvial fan deposits (Li et al., 2022).

168 Stratigraphic ages of the KH and SB sections are constrained by both magnetostratigraphy
169 and fossil assemblages (Fig. 2) (Kaya et al., 2020; Li et al., 2022). Deposition of these two sections
170 started in the late Early Cretaceous (ca. 110 Ma), with a major hiatus between 37 and 20 Ma, and
171 lasted until ~8 Ma (Fig. 2). The depositional ages of detrital samples collected from the Baldshuan
172 and Chingou formations are relatively well constrained with small uncertainties (<0.5 Ma) (Li et
173 al., 2022), while detrital samples collected from the lower marine sections have generally larger
174 uncertainties up to a few million years (Kaya et al., 2020).

175

176 **3. Methods**

177 **3.1. Samples**

178 Four different types of samples were analyzed for this study (Table 1): 1) Twelve detrital
179 sandstone samples from the KH and SB sections for detrital apatite double dating (fission-track
180 and U-Pb; 11 of the 12 samples) and/or detrital zircon fission-track (6 of the 12 samples) analysis;
181 2) Two granite clasts from the Baldshuan Formation conglomerates for zircon U-Pb and fission-
182 track analysis; 3) Four modern sand samples from tributaries of the Panj River (Obikhumbou, Vanj,

183 Yazgulom, and Bartang) draining the Pamir for detrital apatite double dating (on all 4 samples)
184 and/or detrital zircon fission-track (on 3 of the 4 samples) analysis; 4) Four black shale samples
185 from the Cretaceous strata of the KH section for vitrinite reflectance analysis. Detrital samples
186 were processed using standard mineral separation techniques including gravity, heavy liquid, and
187 magnetic separations to separate and concentrate zircon and apatite grains at both Potsdam
188 University (Germany) and the University of Rennes (France).

189

190 **3.2. Apatite fission-track and U-Pb double dating**

191 **3.2.1. Laboratory analyses**

192 Apatite fission-track (AFT) and U-Pb double dating was performed at GeoSep Services
193 (Idaho, USA) using standard procedures for the laser-ablation inductively-coupled plasma mass
194 spectrometer (LA-ICPMS) method. See Supplementary Text S1 as well as Donelick et al. (2005)
195 for a full description of analytical procedures. Supplementary Tables S1 and S2 record raw data
196 for apatite FT and U-Pb measurements, respectively.

197 **3.2.2. Data processing**

198 To obtain the most reliable apatite fission-track data, we adopted the following processing
199 steps: First, as apatite with low uranium content [U] yields low spontaneous fission-track densities,
200 the revealed tracks can differ significantly depending on the surface etched. We thus excluded
201 apatite with [U] content lower than 2 ppm. Second, two different U content parameters were
202 measured with the LA-ICPMS method (see Supplementary Table S1): $^{238}\text{U}/^{43}\text{Ca}$ and [U] (ppm).
203 Theoretically, these two parameters should exhibit a linear relationship with a $[\text{U}]/(^{238}\text{U}/^{43}\text{Ca})$
204 slope of ~ 190 (Donelick et al., 2005). We considered as acceptable a deviation of $\pm 25\%$ in this
205 slope. Thus, a linear test was enforced to exclude analyses with $[\text{U}]/(^{238}\text{U}/^{43}\text{Ca})$ slopes smaller than

206 142.5 or larger than 237.5. Third, analyses with standard errors larger than 75% of the analyzed
207 values were excluded. Lastly, we also excluded zero-track grains for the purpose of deconvolving
208 the Peak Ages. All four criteria were enforced during data processing for the following discussion.

209 The pooled age and central age, both of which define the “average” age of a group of single-
210 grain FT ages, are routinely calculated for bedrock samples, which record a single cooling event.
211 However, these ages are meaningless for detrital samples with $P(\chi^2)$ close to 0, as when the P -
212 value is lower than 0.05, it indicates that the single-grain FT ages are over-dispersed, and multiple
213 age components exist (Vermeesch, 2019). We, therefore, used the mixture modeling of online
214 software *IsoplotR* (<http://isoplotr.geol.ucsb.edu/isoplotr/>) (Vermeesch, 2018) to deconvolve
215 single-grain FT ages of each sample into multiple age components, which are defined as Peak
216 Ages.

217 Due to the low content of [U], many apatite grains did not yield U-Pb ages or yielded ages
218 with very large errors (Supplementary Table S2). We filtered the apatite U-Pb age data to only
219 include analyses with 2-sigma errors smaller than 75% of the U-Pb age.

220

221 **3.3. Zircon fission-track and U-Pb dating**

222 **3.3.1 Zircon fission-track dating**

223 Zircon fission-track (ZFT) analysis was performed following the external detector method
224 (Gleadow, 1981) at the Low-Temperature Thermochronology Laboratory at the University of Sao
225 Paulo (Brazil). See Supplementary Text S2 for a full description of analytical procedures and
226 Supplementary Table S3 for the raw data of analyzed samples.

227 All the raw data were filtered using the standard error criteria, and all reported single-grain
228 ZFT ages pass this test. As the $P(\chi^2)$ is close to 0 for all ZFT samples, we used the same Peak Age
229 deconvolution method as for the AFT samples described above.

230 **3.3.2 Zircon U-Pb dating**

231 Zircon U-Pb dating was carried out using a Thermo Element 2 single collector inductively
232 coupled plasma-mass spectrometer (LA-ICPMS) coupled to a Photon Machines Analyte G2
233 excimer laser at the Arizona LaserChron Center, University of Arizona (USA) following the
234 method outlined by Gehrels et al. (2008). See Supplementary Text S3 for a full description of
235 analytical and data processing procedures and Table S4 for raw data of analyzed samples.

236

237 **3.4. Compilation of regional detrital fission-track data**

238 **3.4.1. Data sources**

239 In the Tajik Basin and adjacent Pamir, fission-track ages of both detrital and bedrock samples
240 have been published (e.g., Abdulhameed et al., 2020; Carrapa et al., 2014; Chapman et al., 2017;
241 Rutte et al., 2017a; Sobel and Dumitru, 1997; Stübner et al., 2013; Thiede et al., 2013; Wang et
242 al., 2019). To explore the long-term exhumation history of the Pamir, we compiled the following
243 detrital fission-track data sets (see Fig. 1 for locations): 1) detrital apatite FT data of modern river
244 sands from the Pamir (Carrapa et al., 2014); 2) detrital apatite FT data from the PE section (30–23
245 Ma) of the north-central Tajik Basin (Wang et al., 2019); and 3) detrital zircon FT data from the
246 DH section of the eastern Tajik Basin (Chapman et al., 2020). These data sets were combined with
247 the new AFT and ZFT data of this study for further analysis (section 3.4.2). Detrital fission-track
248 data have also been reported from the southwestern Tarim Basin (e.g., Cao et al., 2015; Cao et al.,
249 2013b; Clift et al., 2017; Wang et al., 2021). We did not incorporate these data in the compilation

250 because a significant component of the detritus in these Tarim sections was sourced from the West
251 Kunlun to the south, thus yielding information that may not be directly relevant to the Pamir.

252 **3.4.2. Data processing**

253 To extract the most useful information from the compiled FT ages, we evaluated two
254 different strategies of data processing: either compiling all the single-grain FT ages in Kernel
255 Density Estimate (KDE) plots; or, compiling all the deconvolved Peak Ages to make KDE plots.
256 We chose the second strategy for the following reasons: Single-grain FT ages are not as meaningful
257 as single-grain ages from other methods, such as zircon U-Pb, due to the intrinsic characteristics
258 of FT accumulation resulting in a Poissonian distribution of fission tracks in a crystal (Galbraith,
259 1981). Thus, for bedrock, a “pooled age” is usually used to represent the cooling age; while for
260 detrital samples, each deconvolved Peak Age represents a distinct cooling age in the source
261 terranes (e.g., Vermeesch, 2019). As a result, a compilation of Peak Ages is more meaningful than
262 a compilation of single-grain ages to represent the source terrane cooling ages. Peak Ages that
263 indicate partial annealing, such as those of the two Cretaceous samples from the KH section,
264 amongst others (see detailed discussion in section 5.1), were excluded from the compilation, as
265 these Peak Ages do not represent exhumation ages.

266 The original AFT data of Carrapa et al. (2014) and the ZFT data of Chapman et al. (2020)
267 were reprocessed to derive the deconvolved Peak Ages. As individual Peak Ages may be
268 interpreted to reflect source terrane cooling events (Garver et al., 1999; Ruiz et al., 2004), we
269 plotted the KDE curves for the compiled AFT and ZFT Peak Ages to reflect the intensity and
270 contribution of individual cooling events, similar to common interpretations of detrital zircon U-
271 Pb provenance. The height of the KDE plot peak arguably reflects the intensity of corresponding
272 Peak Ages in the source terrane, i.e., higher KDE peaks indicate stronger cooling events, either

273 regionally more extensive or temporally more intensive, similar to the interpretation of bedrock
274 FT age KDE plots in Jepson et al. (2021).

275 Unlike bedrock FT ages, an issue that needs to be considered when constructing the KDE
276 plots of compiled detrital FT Peak Ages from multiple samples, is the treatment of individual Peak
277 Ages. Each sample considered will have deconvolved Peak Ages represented by a variable number
278 of single-grain ages. Also, Peak Ages defined by a percentage of grains within a sample may
279 represent very different numbers of grains between samples because the total number of analyzed
280 grains differs between samples. Two different ways of accounting for individual Peak Ages can
281 thus be considered. We can simply ignore the percentage represented by each individual Peak Ages
282 in each sample and treat each Peak Age with the same weight when constructing the KDE plots.
283 However, this strategy may over-represent Peak Ages that only occupy a small percentage in each
284 sample. Alternatively, we can determine different weights for different Peak Ages according to
285 their incorporated single-grain age percentage in each sample and treat the weight of each sample
286 the same. Each Peak Age was weighted by values obtained as follows: in each sample, we first
287 divided the percentage of each Peak Age by ten and then rounded the value to their nearest integer.
288 This integer was considered as the weight of the Peak Age. Each Peak Age was then counted
289 multiple times by its weight for the construction of the KDE plots. We consider that this second
290 strategy better represents the source terrane cooling ages, and therefore it was adopted in the
291 following analyses and discussion.

292

293 **3.5. Vitrinite reflectance analysis**

294 Vitrinite reflectance is the proportion of incident light reflected from a polished vitrinite
295 surface (%Ro), which is a proxy of the thermal maturity of organic matter (Taylor et al., 1998).

296 Adopting certain transfer equations, vitrinite reflectance values can be converted to burial
297 temperatures (e.g., Barker and Goldstein, 1990; Nielsen et al., 2017; Sweeney and Burnham, 1990).
298 Four organic-rich shale samples were collected from the Cretaceous marine strata of the KHC
299 section (Fig. 2). The analyses were carried out at the Federal University of Rio Grande do Sul
300 (Brazil). Samples were processed following standard procedures (Bustin et al., 1985) to make
301 plugs for vitrinite reflectivity measurement according to ISO standard 7404-5
302 (<https://www.iso.org/obp/ui/#iso:std:iso:7404:-5:ed-3:v1:en>). For each sample, 34 to 51
303 measurements were made. Following Abdulhameed et al. (2020), we converted the %Ro values to
304 burial temperatures using two different methods: an empirical equation from Barker and Goldstein
305 (1990), and a chemical kinetic model equation from Sweeney and Burnham (1990).

306

307 **4. Results**

308 **4.1. New apatite fission-track ages**

309 All AFT samples fail the χ^2 test, with $P(\chi^2)$ values equal or close to 0 (Supplementary Fig.
310 S1), indicating that these fission-track age distributions are mixtures of different cooling age
311 components (Peak Ages). This is expected for not fully reset detrital FT samples (Ruiz et al., 2004).
312 Significant differences exist concerning the deconvolved Peak Ages between modern river sands
313 and sandstones (Table 2 and Fig. 3). Modern river sand samples are exclusively dominated by Late
314 Oligocene–Early Miocene (P2) and Middle–Late Miocene (P1) populations. Sandstone samples
315 from the KH and SB sections generally show three dominant Peak Age populations during the
316 Early–early Late Cretaceous (P4), Late Cretaceous–early Paleogene (P3), and Late Eocene–Early
317 Miocene (P2), but also with a few Middle–Late Miocene (P1) and Late Jurassic (P5) populations.

318 We emphasize that the deconvolved Peak Ages only change slightly when using different
319 filtering methods as discussed in section 3.2.2, e.g., adopting no filters, or only adopting [U]
320 content and zero-track filters. The differences between deconvolved Peak Ages are small
321 (Supplementary Fig. S2) and exert no influence on the following interpretation and discussion.

322

323 **4.2. New zircon fission-track ages**

324 Similar to the AFT ages, the ZFT ages of all samples have $P(\chi^2)$ values equal or close to 0
325 (Supplementary Fig. S3), indicating mixtures of different cooling age components (Peak Ages). In
326 contrast to the exclusively young AFT Peak Ages, the ZFT ages of modern river sand samples
327 shares similar Peak Age populations to sandstone samples (Table 3 and Fig. 4). In general, there
328 are strong Triassic–Early Jurassic (P5), Early–early Late Cretaceous (P4), Late Cretaceous–early
329 Paleogene (P3), and Late Eocene–Early Miocene (P2) populations, while the Middle–Late
330 Miocene population (P1) is less prominent.

331 As expected for a granite clast in which all the grains experienced a similar cooling history,
332 the two granite clasts from the Baldshuan Formation conglomerates yielded single ZFT Peak Ages
333 (Table 3). Sample TK18-44 (~14 Ma depositional age) recorded a single ZFT Peak Age of ~272
334 Ma, and sample TK18-45 (~18 Ma depositional age) recorded a single ZFT Peak Age of ~212 Ma.

335

336 **4.3. New apatite and zircon U-Pb ages**

337 The majority of apatite U-Pb ages are between 200 and 600 Ma, with another smaller cluster
338 at 30–50 Ma. Due to large uncertainties, we do not discuss the geologic meaning of these single-
339 grain apatite U-Pb ages, but compare them with the double-dated AFT ages in section 5.2.

340 Granite clast sample TK18-45 gave an unanchored zircon U-Pb age of 437 ± 7 Ma, and an
341 anchored age of 447 ± 4 Ma (Supplementary Fig. S4). Both ages overlap within uncertainty at 443
342 Ma. Granite clast sample TK18-44 gave a surprising degree of variability of grain ages between
343 570–2644 Ma (Supplementary Fig. S4). In view of this uncertainty, we use this sample only as
344 supporting evidence, given its single ZFT age (~ 272 Ma) is in agreement with that of granite clast
345 TK18-45 (~ 212 Ma), thus supporting our conclusion regarding the timing of exhumation of the
346 source terrane (section 6.1). Please see Supplementary Text S4 for further discussion of the two
347 zircon U-Pb ages from these two samples.

348

349 **4.4. Regional pattern of detrital fission-track ages**

350 Generally, the Peak Ages of the compiled AFT and ZFT data agree with the new data
351 reported in this study (Figs. 3–4), such that the modern river sand AFT Peak Ages are similar
352 between the western and eastern Pamir rivers; and the ZFT Peak Ages are similar between the
353 KH&SB sections and the DH section of the Tajik Basin (Figs. 3 and 4). Slightly different from the
354 modern river sand AFT data of this study, the modern river sand AFT data reported by Carrapa et
355 al. (2014) have several Mesozoic Peak Ages (Fig. 3); however, it is noted that the percentages of
356 these old Peak Ages are small (e.g., $<5\%$). The other notable differences include: 1) the AFT Peak
357 Ages of the PE section sandstones are dominated by P2 and P3, lacking other Peak Ages (Fig. 3);
358 and 2) the ZFT Peak Ages of the DH section sandstones lack P3 (Fig. 4).

359 The KDE plots of the compiled AFT and ZFT Peak Ages show several distinct peaks (Fig.
360 5A–B). For the AFT Peak Age KDE plot, there is a broad peak between 140 and 90 Ma and a
361 strong peak between 40 and 6 Ma (Fig. 5A), the latter of which can be further subdivided into
362 populations with sub-peaks at ~ 36 Ma, ~ 25 Ma, ~ 14 Ma, and ~ 7 Ma (Fig. 5C). The ZFT Peak Age

363 KDE plot shows four distinguishable peaks at 220–200 Ma, 110–90 Ma, 75–60 Ma, and 40–6 Ma
364 (Fig. 5B), the latter of which also show distinct sub-peaks that are consistent with the populations
365 identified from the AFT Peak Age KDE plot (Fig. 5D).

366 We also compared the KDE plots using the two different Peak Age processing methods
367 discussed in section 3.4.2. The KDE plots show slight differences but possess the same peaks as
368 discussed here (Supplementary Fig. S5).

369

370 **4.5. Burial temperatures**

371 The four vitrinite reflectance (%Ro) values show two groups (Table 4, and Supplementary
372 Fig. S6). The two ~90 Ma samples have %Ro values of 0.44 and 0.50, corresponding to burial
373 temperatures of 54–70 °C or 80–90 °C, depending on the different temperature calibration
374 equations used (Table 4). The other two 97 Ma and 100 Ma samples have %Ro values of 0.61 and
375 0.67, corresponding to burial temperatures of 94–106 °C or 107–114 °C. A burial temperature
376 reported adjacent to our KH section records 75 °C or 94 °C (depending on the two different transfer
377 equations used in Abdulhameed et al., 2020), which is in between the values reported for our upper
378 two and lower two samples in this study.

379

380 **5. Evaluation of fission-track data**

381 **5.1. Influence of burial annealing**

382 The closure temperature of the apatite fission-track system is ~120 °C, and fission tracks will
383 anneal when residing in the partial annealing zone (PAZ) at ~120–60 °C (Green et al., 1989).
384 Similarly, the closure temperature of the zircon fission-track system is ~240 °C, and the PAZ is
385 from ~240–180 °C (Tagami, 2005). Deep burial of sedimentary rocks to their PAZ would reset the

386 primary cooling ages and yield fission-track ages that are useful to explore the thermal history of
387 the basin but do not reflect the timing of exhumation of the grains' source region. Only samples
388 that were shallowly buried and remained above the PAZ after deposition record the original
389 exhumation information of the source terrane.

390 In the studied KH&SB and DH sections, all samples have their ZFT Peak Ages older than
391 depositional ages (i.e., lag-time > 0 Ma; Fig. 6B). With one exception, all Cenozoic samples have
392 their AFT Peak Ages older than depositional ages (Fig. 6A). We, therefore, interpret these Peak
393 Ages as representing the timing of cooling in the source region. The one exception is TK16-11,
394 the P1 of which is younger than its depositional age. We noted that this Peak Age only accounts
395 for 6% of total single grain AFT ages, and a weak positive correlation was also observed between
396 the single grain AFT ages and their Dpar values for this sample (Supplementary Fig. S7),
397 indicating influence of chemical compositions of apatite grains on annealing temperatures (e.g.,
398 Peyton and Carrapa, 2013). We thus interpret this younger than depositional age AFT Peak Age
399 as a result of the resetting of the AFT ages of certain apatite grains, i.e., those with smaller Dpar,
400 which usually have slightly lower partial annealing temperatures (Ketcham et al., 1999).

401 For the two newly collected Cretaceous samples, all their AFT Peak Ages, except one, are
402 younger than depositional ages (Fig. 6A). The presence of more than one Peak Age indicates
403 partial rather than full resetting, which is consistent with vitrinite reflectance data that show burial
404 temperatures of 54–90 °C for the Upper Cretaceous strata, and 94–114 °C for the upper Lower
405 Cretaceous strata (Table 4, considering both transfer equations). These temperatures fall in the
406 range of the AFT PAZ at ~120–60 °C. Both samples show a weak positive correlation of single
407 grain AFT ages vs. Dpar, indicating an influence of mineral chemistry on age distribution (Carlson
408 et al., 1999) (Supplementary Fig. S7).

409

410 **5.2. Contribution of igneous cooling ages**

411 To use detrital FT ages to reflect source terrane exhumation history, the contribution of
412 volcanic and/or plutonic cooling ages should be first excluded, as these ages reflect the timing of
413 shallow intrusion and/or eruption rather than exhumation. In the Pamir, Paleozoic to Eocene
414 igneous rocks have been reported (Chapman et al., 2018b; Schwab et al., 2004). U-Pb and FT
415 double dating on the same grain can help determine whether FT ages represent cooling post-
416 eruption / shallow intrusion (similar U-Pb and FT ages) or are due to exhumation (U-Pb age older
417 than FT age) (Reiners et al., 2005).

418 Fig. 7A shows that for the major exhumation periods that we will discuss in section 6, i.e.,
419 the Early–early Late Cretaceous and the Cenozoic, the majority of grains fall away from the apatite
420 FT versus U-Pb 1:1 line, indicating that the FT ages represent exhumation signals (Reiners et al.,
421 2005). In the DH section (Fig. 1), detrital zircon U-Pb and FT double dating from Chapman et al.
422 (2020) (Fig. 7B) more clearly indicates exhumation signals, because the errors on zircon U-Pb
423 analyses are much smaller than those for apatite.

424

425 **5.3. Consideration of exhumation rates**

426 From old to young (Fig. 6A–B), Peak Age populations P5 (Late Triassic–Early Jurassic), P4
427 (Early–early Late Cretaceous), and P3 (Late Cretaceous–early Paleogene), all have static peaks
428 that show no changes in Peak Ages but increasing lag times (Bernet and Garver, 2005). For P2 of
429 the AFT data, the majority of lag times have values that range between 8–14 Myrs, with an average
430 of 10 Myrs for the Miocene sedimentary rocks (Fig. 6A and Table 2). The lag times of P2 on the
431 ZFT plot (Fig. 6B) are more scattered, mainly between 10–15 Myrs. P2 may represent a moving

432 peak of constant lag time (Fig. 6A–B), indicating steady state exhumation during the Miocene,
433 perhaps with accelerated exhumation to the present as indicated by shorter lag times of some P1
434 modern river sediments. However, this suggestion should be viewed with caution, given that peaks
435 represent input from more than one terrane, and thus can only represent a spatially averaged
436 scenario.

437 Assuming a thermal gradient of ~ 25 °C/km, the long-term exhumation rate in the Pamir
438 during the Miocene, deduced from the compiled detrital FT data of this study, is ~ 0.5 – 1 mm/yr,
439 which generally agrees with the estimated average Cenozoic exhumation rates of 0.6 – 1.3 mm/yr
440 in the Central and South Pamir, but higher than the 0.4 – 0.2 mm/yr rates for the Northeastern Pamir,
441 based on bedrock ^{40}Ar - ^{39}Ar dating (Carrapa et al., 2014).

442 There is one sample (TK16-14, Table 2) showing ~ 1 Myr AFT lag time (AFT Peak Age 1:
443 ~ 17.2 Ma; depositional age: ~ 16.3 Ma). Early Miocene crystallization ages (21 – 16 Ma) were
444 reported from leucogranite from the Pamir gneiss domes (Chapman et al., 2018b; Stearns et al.,
445 2015), hinting that the 17.2 Ma AFT Peak Age may represent igneous cooling and/or volcanic
446 extrusion age. Further examination of single grain apatite FT and U-Pb ages indicates that this is
447 not the case as the majority of grains incorporated in this Peak Age are much older than 25 Ma
448 (Supplementary Fig. S8). We, thus, interpret this very short lag time to represent very high
449 exhumation rate (~ 4 – 5 mm/yr) at 17 – 16 Ma. Exhumation rates as high as >3 mm/yr and 1 – 3 mm/yr
450 were reported from the Central and South Pamir gneiss domes, respectively, both of which are
451 active since ~ 20 Ma (Rutte et al., 2017a; Stübner et al., 2013). This is also consistent with
452 exhumation rate estimates from modern river sand detrital thermochronology (Carrapa et al., 2014).
453 The fact that this very short lag-time was only found in one of the samples argues for the short
454 duration of the ~ 17 – 16 Ma intense exhumation event represented by this Peak Age.

455

456 **6. Mesozoic–Cenozoic tectonic evolution and formation of the Pamir**

457 **6.1. Provenance of the grains dated by fission-track analyses**

458 As argued in the last section (5), the deconvolved Peak Ages of detrital fission-track samples
459 reflect the long-term exhumation history of the source terranes. Before discussing the exhumation
460 history, we first need to identify the source terranes of these apatite and zircon grains. In the eastern
461 Tajik Basin, including the DH, SB, and KH sections, provenance studies, including the use of the
462 detrital zircon U-Pb method, indicate that the Pamir has served as the major detrital source since
463 the Cretaceous (Chapman et al., 2020; Kaya et al., 2020; Klocke et al., 2017; Li et al., 2022; Wang
464 et al., 2019). Further refinement of our discussion can be attained by determination of which
465 terranes in the Pamir sourced the grains.

466 Leaving aside any issues of potential recycling, modern river sands are the easiest to interpret
467 in this respect, since the source is clear (Fig. 1A), but only provides a modern-day snapshot.
468 Interpretation of detrital samples from older strata is possible where characteristics differ between
469 potential source regions. In the Pamir, Triassic and Paleozoic granites are typical of the North
470 Pamir, Eocene intrusions are typical of the Central Pamir, and Cretaceous intrusions are typical of
471 the South Pamir (Chapman et al., 2018b; Schwab et al., 2004). Our granite conglomerate clasts
472 (samples TK18-44 and 45) are Paleozoic, as determined from zircon U-Pb dating (section 4.3) and
473 we therefore consider them derived from the North Pamir. Double-dated individual grains in the
474 sandstone sections cannot be so readily assigned to a specific terrane since grains from the igneous
475 rocks may have been eroded, transported, and redeposited in sediments on a different terrane; for
476 example, Central and South Pamir Mesozoic sedimentary rocks have a Triassic zircon population
477 although Triassic igneous rocks are not present in this terrane (Li et al., 2022; Villarreal et al.,

478 2020). However, there are limited sedimentary rocks younger than Jurassic in the North Pamir and
479 therefore we are confident to ascribe grains with Cretaceous and Eocene U-Pb ages to the South
480 and Central Pamir, respectively. Eocene grains are recorded in both the KH&SB and DH sections;
481 Cretaceous grains are rare, although the KH section show a few zircons (Fig. 7).

482

483 **6.2. Late Triassic–Early Jurassic Cimmerian orogeny in the Pamir**

484 Our new ZFT data, and almost all the compiled detrital ZFT samples show Late Triassic–
485 Early Jurassic Peak Ages (P5: 170–230 Ma; Fig. 4). On the KDE plot of the compiled ZFT Peak
486 Ages, a peak between 200–230 Ma can also be identified (Fig. 5B). From provenance information,
487 we know that this period of exhumation affected the North Pamir as determined by the Triassic FT
488 ages of the granite conglomerate clasts, and the Central and/or South Pamir as determined from
489 ZFT ages in the modern river sands of the Bartang and possibly also the Vanj rivers which drain
490 the Central and South Pamir (Fig. 1), although the Triassic Peak Age in the latter has large errors
491 (Table 3).

492 Previous studies, which used stratigraphy, geochronology, thermochronology, provenance,
493 and structural methods, inferred broadly synchronous terrane collisions between the North, Central,
494 South Pamir, and Karakoram during the latest Triassic–earliest Jurassic (Angiolini et al., 2013;
495 Imrecke et al., 2019; Robinson, 2015; Villarreal et al., 2020). We thus interpret these Late Triassic–
496 Early Jurassic FT cooling ages to record the exhumation associated with the closure of the Paleo-
497 Tethys Ocean and the ensuing terrane collisions which caused strong deformation along the
498 Tanymas and Rushan-Pashart suture zones during the Cimmerian orogeny.

499 Late Triassic cooling ages have also been documented by detrital samples from the Tian
500 Shan, which was also interpreted to be associated with the Cimmerian collision in the southern

501 Eurasian margin (De Grave et al., 2012). Similar Late Triassic–Early Jurassic detrital zircon FT
502 ages from the West Kunlun, however, were interpreted to reflect the northward subduction of the
503 Paleo-Tethys oceanic lithosphere beneath the West Kunlun (Cao et al., 2015).

504

505 **6.3. Early–early Late Cretaceous rejuvenated deformation in the Pamir**

506 Both AFT and ZFT Peak Ages show strong Early–early Late Cretaceous exhumation signals
507 (P4; Figs. 3–4). The KDE plots show subtle differences between the compiled AFT and ZFT data
508 (Fig. 5): the AFT Peak Age KDE plot has a relatively broad range between 140 Ma and 90 Ma,
509 while the ZFT Peak Age KDE plot has a narrower range between 110 Ma and 90 Ma.

510 We interpret these cooling ages to record exhumation associated with rejuvenated
511 deformation in the Pamir during the Early–early Late Cretaceous. Multiple lines of evidence
512 support this interpretation. In the northeast Pamir, it is inferred that during the Early–early Late
513 Cretaceous, the Karakul-Mazar terrane was imbricated by thrust faults and over-thrusted
514 southward above the Central Pamir (Robinson et al., 2012; Rutte et al., 2017b). Amphibolite facies
515 metamorphism in the Karakul-Mazar terrane was interpreted to be caused by thrust imbrication
516 (Robinson et al., 2004). Thick Cretaceous fluvial rocks in the Tarim and Tajik Basins were
517 interpreted to be deposited in foreland basins and sourced from the Karakul-Mazar terrane
518 (Bershaw et al., 2012; Chapman et al., 2020; Kaya et al., 2020). In the South Pamir, mapping and
519 thermochronology studies document Cretaceous shortening and exhumation (cooling ages: 110–
520 80 Ma) (Chapman et al., 2018a).

521 Based on the observation of synchronous deformation and exhumation in the North and
522 South Pamir, Robinson (2015) suggested that the entire Pamir experienced Early–early Late
523 Cretaceous deformation. During the same time interval, Cretaceous arc magmatism (South Pamir

524 Batholith) occurred in the South Pamir (Aminov et al., 2017; Chapman et al., 2018a). It is thus
525 inferred that the Early–early Late Cretaceous arc magmatism and retro-arc deformation and
526 exhumation in the Pamir were caused by the northward subduction of the Neo-Tethys oceanic
527 lithosphere beneath the Pamir crust (Robinson, 2015). This slab subduction inference seems to be
528 consistent with the suggestion from studies in Tibet that the Neo-Tethys ocean ceased slab rollback
529 and resumed its advance since ~120 Ma, and lasted until ~90 Ma (Kapp and DeCelles, 2019). The
530 strong 110–90 Ma peak of the compiled ZFT Peak Age KDE plot (Fig. 5B) corresponds to the
531 initiation of strong arc magmatism (110–90 Ma, peak at ~104 Ma) in the South Pamir (Aminov et
532 al., 2017; Chapman et al., 2018a), probably suggesting a phase of intense subduction of the Neo-
533 Tethys Ocean. This stage of contractional deformation may have also influenced the Tian Shan
534 and West Kunlun area to cause Early Cretaceous rapid cooling there (Cao et al., 2015; Dumitru et
535 al., 2001; Jepson et al., 2018).

536 From the above, it can be deduced that it is likely that all Pamir terranes were exhuming
537 during this period, although direct evidence for the exhumation of the Central Pamir during this
538 interval has remained elusive. Our modern river ZFT data from the Obikhumbou River draining
539 the North Pamir (TK16-35, Table 3) shows evidence for this phase of exhumation whilst our data
540 from the modern Vanj River (TK16-36) draining the Central Pamir does not. However, such
541 exhumation is hinted at in the Vanj River (TJK8, Table 2) and Gunt River (TJK5) AFT data from
542 Carrapa et al. (2014), which drain the Central Pamir and South Pamir, respectively. Considering
543 the complications of potential recycling of sandstone samples, further ZFT studies of modern river
544 sands from the Central Pamir are needed to more robustly verify whether this Early–early Late
545 Cretaceous exhumation occurred in the Central Pamir.

546

547 **6.4. Late Eocene–Neogene formation of the Pamir**

548 The most prominent peak of the compiled AFT Peak Age KDE plot (Fig. 5A) and the second
549 most prominent peak of the compiled ZFT Peak Age KDE plot (Fig. 5B) is the one in the Cenozoic
550 (e.g., 40–0 Ma). The compiled number of grains contributing to the ZFT Peak Ages is small, which
551 may generate unreliable peaks on the KDE plot. We thus focus the following discussion mainly
552 on AFT ages, but also taking into consideration the ZFT ages.

553 Mainly based on the AFT data, we identified four populations within the 40–0 Ma range with
554 peaks at ~36 Ma, ~25 Ma, ~14 Ma, and ~7 Ma (Fig. 5C). The first three populations are also
555 recorded by ZFT ages (Fig. 5D), while the last population is only recorded in the AFT ages of
556 modern river sand samples (Table 2). This suggests that the last stage of exhumation has not yet
557 eroded deep enough to expose rocks with Late Miocene ZFT ages to the surface. Modern river FT
558 data show that the four exhumation stages we identified are present in the North, Central, and
559 South Pamir (Tables 2 and 3).

560 Our results agree with previous studies documenting Late Eocene–Neogene deformation and
561 exhumation in the Pamir. A Late Oligocene–Early Miocene growth phase of the Pamir has been
562 documented widely in sedimentary records in the surrounding basins (Tajik, Tarim, and Alai)
563 (Blayney et al., 2019; Coutand et al., 2002; Wang et al., 2019). The Middle–Late Miocene
564 exhumation in the Pamir is also echoed in studies that include the appearance of thick
565 conglomerate deposits at 15 Ma and 13.5 Ma in the Tarim and Tajik basins, respectively (Blayney
566 et al., 2019; Li et al., 2022; Zheng et al., 2015) and a significant provenance shift from the Central
567 to the North Pamir denoting a phase of exhumation around 12 Ma (Li et al., 2022).

568 Within the Pamir, significant crustal thickening occurred in the Central Pamir during the Late
569 Eocene and Early Miocene (e.g., >37 Ma to ~20 Ma), which caused prograde metamorphism

570 recorded in Miocene gneiss domes across the region and led to the present-day crustal thickness
571 of $\sim 70 \pm 10$ km (Hacker et al., 2017; Rutte et al., 2017a). Shortly after, significant exhumation of
572 the gneiss domes from middle–lower crustal levels prevailed in the Central Pamir from ~ 22 Ma
573 until ~ 12 Ma and until ~ 4 Ma in the South Pamir (Rutte et al., 2017a; Stübner et al., 2013;
574 Worthington et al., 2020). The Central Pamir dome exhumation possibly reflects the very short
575 lag-time at ~ 17 – 16 Ma observed in one of our samples (Fig. 6A). In the northeastern Pamir,
576 bedrock experienced a stage of accelerated exhumation at 25 – 16 Ma (Amidon and Hynek, 2010;
577 Sobel et al., 2013), and another stage in the Late Miocene–Pliocene associated with the Kongur
578 Shan extensional system (Cao et al., 2013a; Chen and Chen, 2020; Robinson et al., 2004; Sobel et
579 al., 2011; Thiede et al., 2013). In the northwestern Pamir, bedrock AFT ages between 15 Ma and
580 6 Ma, and zircon and apatite (U-Th)/He ages between 26 Ma and 2.5 Ma have also been reported
581 (Abdulhameed et al., 2020; Sobel et al., 2021). AFT studies of modern river sands across the Pamir
582 record strong Miocene–Pliocene signals indicating rapid erosion at the regional scale (Carrapa et
583 al., 2014).

584

585 **7. Conclusions**

586 This study provides both apatite and zircon fission-track data from Cretaceous–Miocene
587 sandstones from the eastern Tajik Basin and modern river sands from the Pamir to explore the
588 Mesozoic–Cenozoic tectonic evolution and formation of the Pamir.

589 Vitritite reflectance data and comparisons between FT ages and depositional ages indicate
590 that the grains experienced negligible partial annealing except for the two lowermost samples in
591 the Cretaceous part of the studied section, which were buried to their AFT partial annealing zone.
592 Double dating further indicates that the majority of FT ages record mostly exhumation signals, and

593 do not represent the timing of shallow intrusion of igneous rocks or extrusion of volcanics. We
594 thus interpret the fission-track data to record their source terrane long-term exhumation history.

595 A compilation of both the new AFT and ZFT data of this study and published detrital fission-
596 track data from the Pamir and Tajik Basin show prominent Mesozoic cooling ages that reflect
597 deformation and exhumation of the Pamir associated with the Late Triassic–Early Jurassic
598 Cimmerian orogeny that collaged the Pamir terranes, as well as the rejuvenated Early–early Late
599 Cretaceous deformation caused by the northward subduction of the Neo-Tethys oceanic
600 lithosphere beneath Pamir. The compiled data set also shows strong exhumation of the Pamir
601 during the Late Eocene–Neogene that peaks at ~36 Ma, ~25 Ma, ~14 Ma, and ~7 Ma.

602

603

604 **Acknowledgments**

605 We would like to thank Chris Mark for providing advice on processing the AFT ages, and
606 Alex Pullen and Ian Millar on the processing of zircon U-Pb data. We thank Yanling Wang and
607 Wai Allen for help with zircon BSE imaging and U-Pb analysis. We would like to thank Alexander
608 Robinson, Xin Wang, and Editor Atle Rotevatn for constructive comments and suggestions that
609 helped clarify the contents of this study. This study is supported by the European Research Council
610 consolidator grant MAGIC 649081 to GDN.

611

612

613 **References**

614 Abdulhameed, S., Ratschbacher, L., Jonckheere, R., Gaḡała, Ł., Enkelmann, E., Käßner, A., Kars,
615 M.S.C., Szulc, A., Kufner, S.K., Schurr, B., 2020. Tajik Basin and Southwestern Tian Shan,

616 Northwestern India-Asia Collision Zone: 2. Timing of Basin Inversion, Tian Shan Mountain
617 Building, and Relation to Pamir-Plateau Advance and Deep India-Asia Indentation. *Tectonics* 39,
618 doi: 10.1029/2019TC005873.

619 Amidon, W.H., Hynek, S.A., 2010. Exhumational history of the north central Pamir. *Tectonics* 29,
620 doi:10.1029/2009TC002589.

621 Aminov, J., Ding, L., Mamadjonov, Y., Dupont-Nivet, G., Aminov, J., Zhang, L.-Y., Yoqubov, S.,
622 Aminov, J., Abdulov, S., 2017. Pamir Plateau formation and crustal thickening before the India-
623 Asia collision inferred from dating and petrology of the 110–92 Ma Southern Pamir volcanic
624 sequence. *Gondwana Research* 51, 310-326.

625 Angiolini, L., Zanchi, A., Zanchetta, S., Nicora, A., Vezzoli, G., 2013. The Cimmerian geopuzzle:
626 new data from South Pamir. *Terra Nova* 25, 352-360.

627 Barker, C.E., Goldstein, R.H., 1990. Fluid-inclusion technique for determining maximum
628 temperature in calcite and its comparison to the vitrinite reflectance geothermometer. *Geology* 18,
629 1003-1006.

630 Bazhenov, M.L., Perroud, H., Chauvin, A., Burtman, V.S., Thomas, J.-C., 1994. Paleomagnetism
631 of Cretaceous red beds from Tadzhikistan and Cenozoic deformation due to India-Eurasia collision.
632 *Earth and Planetary Science Letters* 124, 1-18.

633 Bernet, M., Garver, J.I., 2005. Fission-track analysis of detrital zircon. *Reviews in Mineralogy and*
634 *Geochemistry* 58, 205-237.

635 Bershaw, J., Garzzone, C.N., Schoenbohm, L., Gehrels, G., Tao, L., 2012. Cenozoic evolution of
636 the Pamir plateau based on stratigraphy, zircon provenance, and stable isotopes of foreland basin
637 sediments at Oyttag (Wuyitake) in the Tarim Basin (west China). *Journal of Asian Earth Sciences*
638 44, 136-148.

639 Blayney, T., Dupont-Nivet, G., Najman, Y., Proust, J.N., Meijer, N., Roperch, P., Sobel, E.R.,
640 Millar, I., Guo, Z., 2019. Tectonic evolution of the Pamir recorded in the western Tarim Basin
641 (China): sedimentologic and magnetostratigraphic analyses of the Aertashi section. *Tectonics* 38,
642 doi: 10.1029/2018TC005146.

643 Bosboom, R., Dupont-Nivet, G., Huang, W.T., Yang, W., Guo, Z.J., 2014. Oligocene clockwise
644 rotations along the eastern Pamir: tectonic and paleogeographic implications. *Tectonics* 33, 53-66.

645 Bourgeois, O., Cobbold, P.R., Rouby, D., Thomas, J.C., Shein, V., 1997. Least squares restoration
646 of Tertiary thrust sheets in map view, Tajik depression, central Asia. *Journal of Geophysical*
647 *Research: Solid Earth* 102, 27553-27573.

648 Burtman, V.S., Molnar, P.H., 1993. Geological and geophysical evidence for deep subduction of
649 continental crust beneath the Pamir. *Geological Society of America special publication*, 281, doi:
650 10.1130/SPE281-p1.

651 Bustin, R.M., Cameron, A.R., Grieve, D.A., Kalkreuth, W.D., 1985. *Coal Petrology - its principles,*
652 *methods, and applications.* Geological Association of Canada, Victoria.

653 Cao, K., Bernet, M., Wang, G.-C., van der Beek, P., Wang, A., Zhang, K.-X., Enkelmann, E.,
654 2013a. Focused Pliocene–Quaternary exhumation of the Eastern Pamir domes, western China.
655 *Earth and Planetary Science Letters* 363, 16-26.

656 Cao, K., Wang, G.-C., Bernet, M., van der Beek, P., Zhang, K.-X., 2015. Exhumation history of
657 the West Kunlun Mountains, northwestern Tibet: Evidence for a long-lived, rejuvenated orogen.
658 *Earth and Planetary Science Letters* 432, 391-403.

659 Cao, K., Wang, G.-C., van der Beek, P., Bernet, M., Zhang, K.-X., 2013b. Cenozoic thermo-
660 tectonic evolution of the northeastern Pamir revealed by zircon and apatite fission-track
661 thermochronology. *Tectonophysics* 589, 17-32.

662 Carlson, W.D., Donelick, R.A., Ketcham, R.A., 1999. Variability of apatite fission-track annealing
663 kinetics: I. Experimental results. *American mineralogist* 84, 1213-1223.

664 Carrapa, B., Mustapha, F.S., Cosca, M., Gehrels, G., Schoenbohm, L.M., Sobel, E.R., DeCelles,
665 P.G., Russell, J., Goodman, P., 2014. Multisystem dating of modern river detritus from Tajikistan
666 and China: Implications for crustal evolution and exhumation of the Pamir. *Lithosphere* 6, 443-
667 455.

668 Chapman, J.B., Carrapa, B., Ballato, P., DeCelles, P.G., Worthington, J., Oimahmadov, I., Gadoev,
669 M., Ketcham, R., 2017. Intracontinental subduction beneath the Pamir Mountains: Constraints
670 from thermokinematic modeling of shortening in the Tajik fold-and-thrust belt. *GSA Bulletin* 129,
671 1450-1471.

672 Chapman, J.B., Carrapa, B., DeCelles, P.G., Worthington, J., Mancin, N., Cobiainchi, M., Stoica,
673 M., Wang, X., Gadoev, M., Oimahmadov, I., 2020. The Tajik Basin: a composite record of
674 sedimentary basin evolution in response to tectonics in the Pamir. *Basin Research*, doi:
675 10.1111/bre.12381.

676 Chapman, J.B., Robinson, A.C., Carrapa, B., Villarreal, D., Worthington, J., DeCelles, P.G., Kapp,
677 P., Gadoev, M., Oimahmadov, I., Gehrels, G., 2018a. Cretaceous shortening and exhumation
678 history of the South Pamir terrane. *Lithosphere* 10, 494-511.

679 Chapman, J.B., Scoggin, S.H., Kapp, P., Carrapa, B., Ducea, M.N., Worthington, J., Oimahmadov,
680 I., Gadoev, M., 2018b. Mesozoic to Cenozoic magmatic history of the Pamir. *Earth and Planetary*
681 *Science Letters* 482, 181-192.

682 Chen, S., Chen, H., 2020. Late Cenozoic Activity of the Tashkurgan Normal Fault and
683 Implications for the Origin of the Kongur Shan Extensional System, Eastern Pamir. *Journal of*
684 *Earth Science* 31, 723-734.

685 Clift, P.D., Zheng, H., Carter, A., Böning, P., Jonell, T.N., Schorr, H., Shan, X., Pahnke, K., Wei,
686 X., Rittenour, T., 2017. Controls on erosion in the western Tarim Basin: Implications for the uplift
687 of northwest Tibet and the Pamir. *Geosphere* 13, 1747-1765.

688 Coutand, I., Strecker, M., Arrowsmith, J., Hilley, G., Thiede, R., Korjenkov, A., Omuraliev, M.,
689 2002. Late Cenozoic tectonic development of the intramontane Alai Valley,(Pamir-Tien Shan
690 region, central Asia): An example of intracontinental deformation due to the Indo - Eurasia
691 collision. *Tectonics* 21, 6, doi:10.1029/2002TC001358.

692 De Grave, J., Glorie, S., Ryabinin, A., Zhimulev, F., Buslov, M., Izmer, A., Elburg, M., Vanhaecke,
693 F., 2012. Late Palaeozoic and Meso-Cenozoic tectonic evolution of the southern Kyrgyz Tien Shan:
694 Constraints from multi-method thermochronology in the Trans-Alai, Turkestan-Alai segment and
695 the southeastern Ferghana Basin. *Journal of Asian Earth Sciences* 44, 149-168.

696 Dedow, R., Franz, M., Szulc, A., Schneider, J.W., Brückner, J., Ratschbacher, L., Gągała, Ł.,
697 Ringenbach, J.C., Rajabov, N., Gadoev, M., 2020. Tajik Basin and Southwestern Tian Shan,
698 Northwestern India-Asia Collision Zone: 3. Pre-to Syn-orogenic Retro-foreland Basin Evolution
699 in the Eastern Tajik Depression and Linkage to the Pamir Hinterland. *Tectonics* 38, doi:
700 10.1029/2019TC005874.

701 Donelick, R.A., O'Sullivan, P.B., Ketcham, R.A., 2005. Apatite fission-track analysis. *Reviews in*
702 *Mineralogy and Geochemistry* 58, 49-94.

703 Dumitru, T.A., Zhou, D., Chang, E.Z., Graham, S.A., Hendrix, M.S., Sobel, E.R., Carroll, A.R.,
704 2001. Uplift, exhumation, and deformation in the Chinese Tian Shan. *Geological Society of*
705 *America Memoir* 194, 71-99.

706 Gągała, Ł., Ratschbacher, L., Ringenbach, J.C., Kufner, S.K., Schurr, B., Dedow, R.,
707 Abdulhameed, S., Le Garzic, E., Gadoev, M., Oimahmadov, I., 2020. Tajik Basin and

708 Southwestern Tian Shan, Northwestern India-Asia Collision Zone: 1. Structure, Kinematics, and
709 Salt-tectonics in the Tajik Fold-and-thrust Belt of the Western Foreland of the Pamir. *Tectonics*
710 39, doi: 10.1029/2019TC005871.

711 Galbraith, R.F., 1981. On statistical models for fission track counts. *Journal of the International*
712 *Association for Mathematical Geology* 13, 471-478.

713 Gallagher, K., Brown, R., Johnson, C., 1998. Fission track analysis and its applications to
714 geological problems. *Annual Review of Earth and Planetary Sciences* 26, 519-572.

715 Garver, J.I., Brandon, M.T., Roden-Tice, M., Kamp, P.J.J., 1999. Exhumation history of orogenic
716 highlands determined by detrital fission-track thermochronology. *Geological Society, London,*
717 *Special Publications* 154, 283-304.

718 Gehrels, G.E., Valencia, V.A., Ruiz, J., 2008. Enhanced precision, accuracy, efficiency, and spatial
719 resolution of U-Pb ages by laser ablation–multicollector–inductively coupled plasma–mass
720 spectrometry. *Geochemistry, Geophysics, Geosystems* 9, Q03017, doi:10.1029/2007GC001805.

721 Gleadow, A.J.W., 1981. Fission-track dating methods: what are the real alternatives? *Nuclear*
722 *Tracks* 5, 3-14.

723 Green, P., Duddy, I., Laslett, G., Hegarty, K., Gleadow, A.W., Lovering, J., 1989. Thermal
724 annealing of fission tracks in apatite 4. Quantitative modelling techniques and extension to
725 geological timescales. *Chemical Geology: Isotope Geoscience Section* 79, 155-182.

726 Hacker, B.R., Ratschbacher, L., Rutte, D., Stearns, M.A., Malz, N., Stübner, K., Kylander-Clark,
727 A.R., Pfänder, J.A., Everson, A., 2017. Building the Pamir–Tibet Plateau—Crustal stacking,
728 extensional collapse, and lateral extrusion in the Pamir: 3. Thermobarometry and Petrochronology
729 of Deep Asian Crust. *Tectonics* 36, doi:10.1002/2017TC004488.

730 He, J., Kapp, P., Chapman, J.B., DeCelles, P.G., Carrapa, B., 2018. Structural setting and detrital
731 zircon U–Pb geochronology of Triassic–Cenozoic strata in the eastern Central Pamir, Tajikistan.
732 Geological Society, London, Special Publications 483, SP483. 411.

733 Heermance, R.V., Pearson, J., Moe, A., Langtao, L., Jianhong, X., Jie, C., Richter, F., Garzione,
734 C.N., Junsheng, N., Bogue, S., 2018. Erg deposition and development of the ancestral Taklimakan
735 Desert (western China) between 12.2 and 7.0 Ma. *Geology* 46, 919-922.

736 Imrecke, D.B., Robinson, A.C., Owen, L.A., Chen, J., Schoenbohm, L.M., Hedrick, K.A., Lapen,
737 T.J., Li, W.Q., Yuan, Z.D., 2019. Mesozoic evolution of the eastern Pamir. *Geosphere*
738 doi.org/10.1130/L1017.1.

739 Jepson, G., Carrapa, B., Gillespie, J., Feng, R., DeCelles, P.G., Kapp, P., Tabor, C.R., Zhu, J.,
740 2021. Climate as the great equalizer of continental-scale erosion. *Geophysical Research Letters*,
741 e2021GL095008.

742 Jepson, G., Glorie, S., Konopelko, D., Mirkamalov, R., Danišik, M., Collins, A.S., 2018. The low-
743 temperature thermo-tectonic evolution of the western Tian Shan, Uzbekistan. *Gondwana Research*
744 64, 122-136.

745 Jia, Y., Glotzbach, C., Lü, L., Ehlers, T.A., 2021. Cenozoic Tectono-Geomorphologic Evolution
746 of the Pamir-Tian Shan Convergence Zone: Evidence From Detrital Zircon U-Pb Provenance
747 Analyses. *Tectonics* 40, e2020TC006345.

748 Kapp, P., DeCelles, P.G., 2019. Mesozoic–Cenozoic geological evolution of the Himalayan-
749 Tibetan orogen and working tectonic hypotheses. *American Journal of Science* 319, 159-254.

750 Kaya, M.Y., Dupont-Nivet, G., Proust, J.N., Roperch, P., Meijer, N., Frieling, J., Fioroni, C.,
751 Özkan Altiner, S., Stoica, M., Aminov, J., 2020. Cretaceous Evolution of the Central Asian Proto-

752 Paratethys Sea: Tectonic, Eustatic, and Climatic Controls. *Tectonics* 39,
753 doi.org/10.1029/2019TC005983.

754 Ketcham, R.A., Donelick, R.A., Carlson, W.D., 1999. Variability of apatite fission-track annealing
755 kinetics: III. Extrapolation to geological time scales. *American Mineralogist* 84, 1235-1255.

756 Klocke, M., Voigt, T., Kley, J., Pfeifer, S., Rocktäschel, T., Keil, S., Gaupp, R., 2017. Cenozoic
757 evolution of the Pamir and Tien Shan Mountains reflected in syntectonic deposits of the Tajik
758 Basin. *Geological Society, London, Special Publications* 427, 523-564.

759 Kufner, S.-K., Kakar, N., Bezada, M., Bloch, W., Metzger, S., Yuan, X., Mechie, J., Ratschbacher,
760 L., Murodkulov, S., Deng, Z., 2021. The Hindu Kush slab break-off as revealed by deep structure
761 and crustal deformation. *Nature communications* 12, 1-11.

762 Kufner, S.-K., Schurr, B., Sippl, C., Yuan, X., Ratschbacher, L., Ischuk, A., Murodkulov, S.,
763 Schneider, F., Mechie, J., Tilmann, F., 2016. Deep India meets deep Asia: Lithospheric indentation,
764 delamination and break-off under Pamir and Hindu Kush (Central Asia). *Earth and Planetary
765 Science Letters* 435, 171-184.

766 Leven, E.J., 1995. Permian and Triassic of the Rushan-Pshart Zone (Pamir). *Riv. Ital. Paleontol.
767 Stratigr* 101, 3-16.

768 Li, L., Dupont-Nivet, G., Najman, Y., Kaya, M., Meijer, N., Pujol, M., Aminov, J., 2022. Middle
769 to late Miocene growth of the North Pamir. *Basin Research* doi:10.1111/bre.12629.

770 Nielsen, S.B., Clausen, O.R., McGregor, E., 2017. basin% Ro: A vitrinite reflectance model
771 derived from basin and laboratory data. *Basin Research* 29, 515-536.

772 Ogg, J.G., 2012. Geomagnetic Polarity Time Scale, in: Gradstein, F.M., Ogg, J.G., Schmitz, M.,
773 Ogg, G. (Eds.), *The Geological Time Scale 2012*. Elsevier, Amsterdam, pp. 85-113.

774 Peyton, S.L., Carrapa, B., 2013. An Introduction to Low-temperature Thermochronologic
775 Techniques, Methodology, and Applications, in: Knight, C., Cuzella, J. (Eds.), Application of
776 structural methods to Rocky Mountain hydrocarbon exploration and development. AAPG Studies
777 in Geology 65, pp. 15-36.

778 Pozzi, J.-P., Feinberg, H., 1991. Paleomagnetism in the Tajikistan: Continental shortening of
779 European margin in the Pamirs during Indian Eurasian collision. Earth and Planetary Science
780 Letters 103, 365-378.

781 Reiners, P., Campbell, I., Nicolescu, S., Allen, C., Hourigan, J., Garver, J., Mattinson, J., Cowan,
782 D., 2005. (U-Th)/(He-Pb) double dating of detrital zircons. American Journal of Science 305, 259-
783 311.

784 Rembe, J., Sobel, E.R., Kley, J., Zhou, R., Thiede, R., Chen, J., 2021. The Carboniferous Arc of
785 the North Pamir. Lithosphere 2021, 6697858.

786 Robinson, A.C., 2015. Mesozoic tectonics of the Gondwanan terranes of the Pamir plateau. Journal
787 of Asian Earth Sciences 102, 170-179.

788 Robinson, A.C., Ducea, M., Lapen, T.J., 2012. Detrital zircon and isotopic constraints on the
789 crustal architecture and tectonic evolution of the northeastern Pamir. Tectonics 31,
790 doi:10.1029/2011TC003013,.

791 Robinson, A.C., Yin, A., Manning, C.E., Harrison, T.M., Zhang, S.-H., Wang, X.-F., 2004.
792 Tectonic evolution of the northeastern Pamir: Constraints from the northern portion of the
793 Cenozoic Kongur Shan extensional system, western China. Geological Society of America
794 Bulletin 116, 953-973.

795 Ruiz, G.M.H., Seward, D., Winkler, W., 2004. Detrital thermochronology—a new perspective on
796 hinterland tectonics, an example from the Andean Amazon Basin, Ecuador. *Basin Research* 16,
797 413-430.

798 Rutte, D., Ratschbacher, L., Khan, J., Stübner, K., Hacker, B.R., Stearns, M.A., Enkelmann, E.,
799 Jonckheere, R., Pfänder, J.A., Sperner, B., 2017a. Building the Pamir-Tibetan Plateau—Crustal
800 stacking, extensional collapse, and lateral extrusion in the Central Pamir: 2. Timing and rates.
801 *Tectonics* 36, 385-419.

802 Rutte, D., Ratschbacher, L., Schneider, S., Stübner, K., Stearns, M.A., Gulzar, M.A., Hacker, B.R.,
803 2017b. Building the Pamir-Tibetan Plateau—Crustal stacking, extensional collapse, and lateral
804 extrusion in the Central Pamir: 1. Geometry and kinematics. *Tectonics* 36, 342-384.

805 Schmidt, J., Hacker, B.R., Ratschbacher, L., Stübner, K., Stearns, M., Kylander-Clark, A., Cottle,
806 J.M., Alexander, A., Webb, G., Gehrels, G., 2011. Cenozoic deep crust in the Pamir. *Earth and*
807 *Planetary Science Letters* 312, 411-421.

808 Schneider, F., Yuan, X., Schurr, B., Mechie, J., Sippl, C., Haberland, C., Minaev, V., Oimahmadov,
809 I., Gadoev, M., Radjabov, N., 2013. Seismic imaging of subducting continental lower crust
810 beneath the Pamir. *Earth and Planetary Science Letters* 375, 101-112.

811 Schwab, M., Ratschbacher, L., Siebel, W., McWilliams, M., Minaev, V., Lutkov, V., Chen, F.,
812 Stanek, K., Nelson, B., Frisch, W., 2004. Assembly of the Pamirs: Age and origin of magmatic
813 belts from the southern Tien Shan to the southern Pamirs and their relation to Tibet. *Tectonics* 23,
814 doi:10.1029/2003TC001583.

815 Searle, M., Hacker, B., 2018. Structural and metamorphic evolution of the Karakoram and Pamir
816 following India–Kohistan–Asia collision. Geological Society, London, Special Publications 483,
817 doi.org/10.1144/SP483.6.

818 Sippl, C., Schurr, B., Tynpel, J., Angiboust, S., Mechie, J., Yuan, X., Schneider, F., Sobolev, S.,
819 Ratschbacher, L., Haberland, C., 2013. Deep burial of Asian continental crust beneath the Pamir
820 imaged with local earthquake tomography. *Earth and Planetary Science Letters* 384, 165-177.

821 Sobel, E.R., Chen, J., Schoenbohm, L.M., Thiede, R., Stockli, D.F., Sudo, M., Strecker, M.R.,
822 2013. Oceanic-style subduction controls late Cenozoic deformation of the Northern Pamir orogen.
823 *Earth and Planetary Science Letters* 363, 204-218.

824 Sobel, E.R., Dumitru, T.A., 1997. Thrusting and exhumation around the margins of the western
825 Tarim basin during the India-Asia collision. *Journal of Geophysical Research* 102, 5043-5063.

826 Sobel, E.R., Schoenbohm, L.M., Chen, J., Thiede, R., Stockli, D.F., Sudo, M., Strecker, M.R.,
827 2011. Late Miocene–Pliocene deceleration of dextral slip between Pamir and Tarim: Implications
828 for Pamir orogenesis. *Earth and Planetary Science Letters* 304, 369-378.

829 Sobel, E.R., Thiede, R., Ballato, P., Stübner, K., Kley, J., Rembe, J., Gadoev, M., Oimahmadov,
830 I., Strecker, M., 2021. Uplift and growth of the northwest Pamir. EGU General Assembly
831 Conference Abstracts EGU21-10405.

832 Stearns, M., Hacker, B., Ratschbacher, L., Rutte, D., Kylander - Clark, A., 2015. Titanite
833 petrochronology of the Pamir gneiss domes: Implications for middle to deep crust exhumation and
834 titanite closure to Pb and Zr diffusion. *Tectonics* 34, 784-802.

835 Stearns, M.A., Hacker, B.R., Ratschbacher, L., Lee, J., Cottle, J.M., Kylander-Clark, A., 2013.
836 Synchronous Oligocene–Miocene metamorphism of the Pamir and the north Himalaya driven by
837 plate-scale dynamics. *Geology* 41, 1071-1074.

838 Stübner, K., Ratschbacher, L., Weise, C., Chow, J., Hofmann, J., Khan, J., Rutte, D., Sperner, B.,
839 Pfänder, J.A., Hacker, B.R., 2013. The giant Shakh dara migmatitic gneiss dome, Pamir, India-
840 Asia collision zone: 2. Timing of dome formation. *Tectonics* 32, 1404-1431.

841 Sweeney, J.J., Burnham, A.K., 1990. Evaluation of a simple model of vitrinite reflectance based
842 on chemical kinetics. AAPG bulletin 74, 1559-1570.

843 Tagami, T., 2005. Zircon fission-track thermochronology and applications to fault studies.
844 Reviews in Mineralogy and Geochemistry 58, 95-122.

845 Taylor, G.H., Teichmüller, M., Davis, A., Diessel, C.F.K., Littke, R., Robert, P., 1998. Organic
846 petrology. Schweizerbart Science Publishers, Berlin.

847 Thiede, R.C., Sobel, E.R., Chen, J., Schoenbohm, L.M., Stockli, D.F., Sudo, M., Strecker, M.R.,
848 2013. Late Cenozoic extension and crustal doming in the India-Eurasia collision zone: New
849 thermochronologic constraints from the NE Chinese Pamir. Tectonics 32, 763-779.

850 Thomas, J.C., Chauvin, A., Gapais, D., Bazhenov, M., Perroud, H., Cobbold, P., Burtman, V.,
851 1994. Paleomagnetic evidence for Cenozoic block rotations in the Tadjik depression (Central Asia).
852 Journal of Geophysical Research: Solid Earth 99, 15141-15160.

853 Vermeesch, P., 2018. IsoplotR: A free and open toolbox for geochronology. Geoscience Frontiers
854 9, 1479-1493.

855 Vermeesch, P., 2019. Statistics for Fission-Track Thermochronology, in: Malusà, M.G., Fitzgerald,
856 P.G. (Eds.), Fission-Track Thermochronology and its Application to Geology. Springer
857 International Publishing.

858 Villarreal, D.P., Robinson, A.C., Carrapa, B., Worthington, J., Chapman, J.B., Oimahmadov, I.,
859 Gadoev, M., MacDonald, B., 2020. Evidence for Late Triassic crustal suturing of the Central and
860 Southern Pamir. Journal of Asian Earth Sciences: X 3, doi.org/10.1016/j.jaesx.2019.100024.

861 Wang, P., Liu, D., Li, H., Chevalier, M.-L., Wang, Y., Pan, J., Zheng, Y., Ge, C., Bai, M., Wang,
862 S., 2021. Sedimentary Provenance Changes Constrain the Eocene Initial Uplift of the Central
863 Pamir, NW Tibetan Plateau. Frontiers in Earth Science 9, doi: 10.3389/feart.2021.741194, 826.

864 Wang, X., Carrapa, B., Chapman, J.B., Henriquez, S., Wang, M., Decelles, P.G., Li, Z., Wang, F.,
865 Oimahmadov, I., Gadoev, M., 2019. Parathethys last gasp in central Asia and late Oligocene
866 accelerated uplift of the Pamirs. *Geophysical Research Letters* 46, doi:
867 <https://doi.org/10.1029/2019GL084838>.

868 Wang, X., Carrapa, B., Sun, Y.C., Dettman, D.L., Chapman, J.B., Rugenstein, J.K.C., 2020. The
869 role of the westerlies and orography in Asian hydroclimate since the late Oligocene. *Geology* 48,
870 728-732.

871 Worthington, J.R., Ratschbacher, L., Stübner, K., Khan, J., Malz, N., Schneider, S., Kapp, P.,
872 Chapman, J.B., Stevens Goddard, A., Brooks, H.L., 2020. The Alichur dome, South Pamir,
873 western India–Asia collisional zone: detailing the Neogene Shakh dara–Alichur syn-collisional
874 gneiss - dome complex and connection to lithospheric processes. *Tectonics* 39, doi:
875 10.1029/2019TC005735.

876 Zanchi, A., Gaetani, M., 2011. The geology of the Karakoram range, Pakistan: the new 1: 100,000
877 geological map of Central-Western Karakoram. *Italian Journal of Geosciences* 130, 161-262.

878 Zhang, S.J., Hu, X.M., Garzanti, E., 2019. Paleocene initial indentation and early growth of the
879 Pamir as recorded in the western Tarim Basin. *Tectonophysics* 772,
880 doi.org/10.1016/j.tecto.2019.228207.

881 Zhang, Z., Sun, J., 2020. Cenozoic tectonic rotations in different parts of the NE Pamir:
882 implications for the evolution of the arcuate orogen. *International Journal of Earth Sciences* 109,
883 1921-1939.

884 Zheng, H.B., Wei, X.C., Tada, R., Clift, P.D., Wang, B., Jourdan, F., Wang, P., He, M.Y., 2015.
885 Late oligocene–early miocene birth of the Taklimakan Desert. *Proceedings of the National*
886 *Academy of Sciences* 112, 7662-7667.

887 **Figure captions**

888 **Figure 1. (A)** Simplified tectonic map of the Pamir and surrounding regions, showing major
889 terranes, suture zones (black curves), faults (red curves), rivers (blue curves), and gneiss domes
890 (orange patches). Circles and stars represent sandstone and modern river sand samples,
891 respectively: yellow, new samples of this study; blue, samples from earlier studies (Carrapa et al.,
892 2014; Chapman et al., 2020; Wang et al., 2019). Abbreviations: KYTS, Kashgar-Yecheng transfer
893 system; MPT, Main Pamir Thrust; RPS, Rushan-Pshart suture; TS, Taymas suture; TBZ, Tirich-
894 Mir boundary zone. **Inset:** The dashed box shows the location of the main figure, TB, Tajik Basin;
895 HK, Hindu Kush. **(B)** Geologic map of the study area, adapted from Dedow et al. (2020). Black
896 solid curves are measured sections of this study: KH, Khirmanjo section; SB, Shurobod section;
897 Black dashed curve is the previously studied section of Chapman et al. (2020): DH, Dashtijum
898 section. Filled circles represent detrital samples for low-temperature thermochronology studies of
899 this study (orange) and Chapman et al. (2020) (blue).

900

901 **Figure 2.** A simplified and composite stratigraphic section with information on the depositional
902 environments of the studied KH and SB sections in the eastern Tajik Basin (KHN, KHP, and KHC
903 represent the Neogene, Paleogene, and Cretaceous parts of the KH section). Stratigraphic ages and
904 depositional environments are from Kaya et al. (2020) and Li et al. (2022). Note the long
905 depositional hiatus between 37 and 20 Ma. The Global Polarity Time Scale (GPTS) is from Ogg
906 (2012); the right column shows samples analyzed in this study.

907

908 **Figure 3.** Compilation of deconvolved AFT Peak Ages from sandstones from the eastern Tajik
909 Basin and modern river sands from the Pamir. Horizontal gray bars are 1σ errors. Black arrows

910 indicate Peak Ages with <5% of single-grain AFT ages. P1–P5 are Peak Age populations shown
911 in Table 2.

912

913 **Figure 4.** Compilation of deconvolved ZFT Peak Ages from sandstones from the eastern Tajik
914 Basin and modern river sands from the Pamir. Horizontal gray bars are 1σ errors. Black arrows
915 indicate Peak Ages with <5% of single-grain ZFT ages. P1–P5 are Peak Age populations shown
916 in Table 3.

917

918 **Figure 5.** Kernel density estimate (KDE) plots (red curves) and histograms (vertical gray bars) of
919 compiled AFT and ZFT Peak Ages. The upper panel (**A–B**) shows all data points (kernel
920 bandwidth and histogram bin width are both 5 Ma) while the middle panel (**C–D**) shows <80 Ma
921 data points (kernel bandwidth and histogram bin width are both 2 Ma).

922

923 **Figure 6.** Lag-time plots of (**A**) AFT Peak Ages and (**B**) ZFT Peak Ages of the KH & SB & DH
924 sections of eastern Tajik Basin and modern river sands of the Pamir rivers. NP, CP, and SP
925 represent the North, Central, and South Pamir, respectively.

926

927 **Figure 7.** Apatite U-Pb ages vs. AFT ages (**A**) and zircon U-Pb ages vs. ZFT ages (**B**) of the DH
928 section. Each point represents a single grain.

Table 1. Information on newly analyzed samples from this study.

Sample [#]	Type	Stratigraphic heights* / m	Depositional Age / Ma	Latitude (°N)	Longitude (°E)	Analyses methods
18TJS03B	Sandstone	4421	8.0±0.3	37.83257	70.09195	AFT, Ap U-pb, ZFT
18TJS03A	Sandstone	4014	9.0±0.3	37.82774	70.08922	AFT, Ap U-Pb
18TJS02	Sandstone	3573	10.9±0.3	37.82588	70.10375	AFT, Ap U-Pb
TK16-1	Sandstone	3215	11.8±0.3	37.91050	70.11510	AFT, Ap U-Pb
TK18-42	Sandstone	3055	12.1±0.3	37.82238	70.11504	AFT, Ap U-Pb, ZFT
TK16-6	Sandstone	2953	12.4±0.3	37.91137	70.11865	AFT, Ap U-Pb, ZFT
TK16-11	Sandstone	2490	14.0±0.3	37.91246	70.12523	AFT, Ap U-Pb, ZFT
TK16-14	Sandstone	2070	16.3±0.3	37.91227	70.13194	AFT, Ap U-Pb, ZFT
TK16-18	Sandstone	1600	19.8±0.3	37.90847	70.13939	AFT, Ap U-Pb
18TJS07	Sandstone	1560	38±2	37.90783	70.14090	ZFT
TK16-28	Sandstone	880	92±2	37.90738	70.14846	AFT, Ap U-Pb
TK16-32	Sandstone	280	105±2	37.90621	70.15749	AFT, Ap U-Pb
TK18-44	Granite clast	2300	14.3±0.3	37.91255	70.12532	ZFT, Zr U-Pb
TK18-45	Granite clast	1850	18.0±0.3	37.90919	70.13778	ZFT, Zr U-Pb
TK16-35	Modern river sand	N.A.	0	38.46206	70.78967	AFT, Ap U-Pb, ZFT
TK16-36	Modern river sand	N.A.	0	38.29811	71.34425	AFT, Ap U-Pb, ZFT
TK16-37	Modern river sand	N.A.	0	38.19075	71.38169	AFT, Ap U-Pb
TK16-38	Modern river sand	N.A.	0	37.92667	71.59753	AFT, Ap U-Pb, ZFT
KRJ16-B-48	Shale	972	90±2	N.A.	N.A.	VF
KRJ16-B-49	Shale	965	90±2	N.A.	N.A.	VF
KRJ-16-B-31	Shale	568	97±2	N.A.	N.A.	VF
KRJ-16-B-P48	Shale	360	100±2	N.A.	N.A.	VF

Notes: AFT, apatite fission-track; ZFT, zircon fission-track; Ap, apatite; Zr, zircon; VF, vitrinite reflectance; N.A. not available.

[#] See Fig. 1 for locations on map.

* See Fig. 2 for stratigraphic heights.

Table 2. Deconvolved Peak Ages for detrital apatite fission-track data from newly collected samples and published data.

Sample	Depositional Age / Ma	N	P1*	P2*	P3*	P4*	P5*	Others*
<u>KH & SB section sandstones, eastern Tajik Basin, this study</u>								
18TJS03B	8.0±0.3	50	-	-	60.0±4.8 (39%)	136.6±6.6 (61%)	-	-
18TJS03A	9.0±0.3	56	-	19.5±5.5 (10%)	-	131.0±2.8 (90%)	-	-
18TJS02	10.9±0.3	49	-	25.1±2.3 (23%)	61.0±4.3 (26%)	120.1±4.4 (51%)	-	-
TK16-1	11.8±0.3	67	-	-	56.5±3.4 (26%)	108.9±3.7 (46%)	203.3±10.2 (28%)	-
TK18-42	12.1±0.3	65	-	20.9±2.7 (12%)	46.9±3.1 (24%)	93.7±2.9 (42%)	160.8±7.2 (22%)	-
TK16-6	12.4±0.3	78	-	21.6±3.2 (8%)	-	93.3±2.7 (53%)	160.1±5.5 (39%)	-
TK16-11	14.0±0.3	72	11.2±1.7 (6%)	-	44.2±3.1 (10%)	94.8±3.3 (39%)	-	137.1±4.7 (45%)
TK16-14	16.3±0.3	83	-	17.2±0.9 (57%)	66.4±3.3 (21%)	114±3.1 (22%)	-	-
TK16-18	19.8±0.3	55	-	27.8±2.2 (54%)	-	109.3±2.9 (46%)	-	-
TK16-28	92±2	70	5.7±1.7 (12%)	-	50.4±3.2 (46%)	110.9±3.0 (42%)	-	-
TK16-32	105±2	54	7.1±0.5 (69%)	30.0±2.7 (19%)	84.0±4.5 (12%)	-	-	-
<u>Modern river sands, western Pamir, this study[†]</u>								
TK16-35 (NP)	0	66	13.4 (55%)	24.8 (45%)	-	-	-	-
TK16-36 (CP)	0	67	9.3±0.6 (87%)	22.0±2.4 (13%)	-	-	-	-
TK16-37 (CP)	0	43	6.3±0.5 (50%)	-	-	-	-	15.3±1.7 (50%)
TK16-38 (CP/SP)	0	31	6.9±0.8 (84%)	22.1±5.7 (16%)	-	-	-	-
<u>Modern river sands, Pamir, reprocessed data from Carrapa et al. (2014)[†]</u>								
TJK4 (CP)	0	100	14.4±0.7 (69%)	25.3±2.1 (30%)	-	-	161.7±65.4 (1%)	-
TJK5 (SP)	0	102	11.0±0.6 (60%)	16.7±1.2 (38%)	-	103.2±18.7 (2%)	-	-
TJK6 (CP/SP)	0	100	-	16.9±0.5 (100%)	-	-	-	-
TJK7 (CP)	0	100	11.7±0.5 (59%)	27.2±1.4 (36%)	86.4±7.2 (5%)	-	-	-
TJK8 (CP)	0	100	15.3±0.6 (76%)	35.7±3.0 (23%)	-	130.3±42.0 (1%)	-	-
1071-1 (NP)	0	100	13.2±1.1 (13%)	22.5±1.5 (37%)	-	-	-	35.5±1.4 (50%)
1071-2 (NP)	0	100	6.7±0.5 (39%)	33.5±1.4 (35%)	-	-	-	16.5±2.1 (26%)
1071-3 (NP)	0	100	6.8±0.7 (26%)	-	44.7±3.5 (16%)	-	-	15.1±0.9 (59%)
1071-4 (NP)	0	100	-	22.2±0.6 (100)	-	-	-	-
1071-6 (NP)	0	42	12.5±1.1 (43%)	26.1±1.9 (45%)	86.8±9.3 (12%)	-	-	-
1071-7 (NP)	0	100	12.9±0.7 (66%)	23.3±1.6 (35%)	-	-	-	-

Note: N, number of grains accepted; P1–P5 are Peak Age Populations, which group similar FT Peak Ages together. When there is more than one Peak Ages that fell into a specific population, the Peak Age with a smaller percentage of single-grain ages was categorized as “Others”.

* Numbers in brackets represent percentages of single-grain ages in each sample. Dividing the percentages by 10 and then rounding them to their nearest integer derive the weights of individual Peak Ages (0 to 10) as discussed in section 3.4.2 (e.g., 39% would derive a weight of 4).

[†] NP/CP/SP, indicates rivers draining the North, Central, and South Pamir respectively.

Table 3. Deconvolved Peak Ages for detrital zircon fission-track data from newly collected samples and published data.

Sample	Depositional Age / Ma #	N	P1*	P2*	P3*	P4*	P5*	Others*
<u>KH & SB section sandstones, eastern Tajik Basin, this study</u>								
18TJS03B	8.0±0.3	20	-	-	73.6±22.8 (10%)	-	217.9±12.9 (90%)	-
TK18-42	12.1±0.3	20	9.6±4.8 (5%)	-	82.6±13.0 (18%)	-	228.1±15.2 (77%)	-
TK16-6	12.4±0.3	27	-	-	-	101.4±6.2 (82%)	-	266.8±39.6 (18%)
TK16-11	14.0±0.3	40	-	37.8±5.5 (8%)	-	90.8±3.6 (70%)	215.5±18.9 (22%)	-
TK16-14	16.3±0.3	36	-	35.2±3.0 (21%)	61.0±2.4 (79%)	-	-	-
18TJS07	38±2	20	-	-	68.4±5.9 (56%)	-	-	359.8±59.9 (44%)
<u>KH section granite clasts, eastern Tajik Basin, this study</u>								
TK18-44	14.3±0.3	20	-	-	-	-	-	272.3±18.0 (100%)
TK18-45‡	18.0±0.3	18	-	-	-	-	212.3±14.7 (100%)	-
<u>Modern river sands, western Pamir, this study†</u>								
TK16-35 (NP)	0	61	-	18.2±2.0 (13%)	70.3±8.8 (36%)	135.5±9.4 (51%)	-	-
TK16-36 (CP)	0	35	11.5±1.5 (27%)	24.2±2.0 (56%)	52.5±5.3 (14%)	-	211.0±66.2 (3%)	-
TK16-38 (CP/SP)	0	56	-	18.6±1.4 (56%)	-	-	194.9±17.3 (16%)	35.5±3.1 (28%)
<u>DH section sandstones, eastern Tajik Basin, reprocessed data from Chapman et al. (2020)</u>								
DSH5090	7.5±1.0	90	-	16.2±0.8 (38%)	41.1±3.3 (11%)	92.2±4.1 (31%)	204.5±10 (20%)	-
DSH3469	13.0±1.0	57	-	20.0±1.5 (22%)	-	95.5±3.1 (61%)	180.0±10.2 (17%)	-
DSH3164	13.5±1.0	109	-	24.7±1.3 (20%)	-	101.2±2.7 (61%)	226.9±10.5 (19%)	-
DSH2566	17.0±1.0	91	-	31.3±1.9 (20%)	-	108.7±5.0 (59%)	203.4±14.0 (21%)	-
DSH2225	17.5±1.0	83	-	27.5±1.1 (42%)	-	96.0±3.8 (45%)	-	162.9±13.1 (13%)
DSH470	100±3.0	87	-	-	-	103.0±2.9 (76%)	204.4±11.6 (24%)	-

Note: N, number of grains accepted; P1–P5, Peak Age Populations, see definition in Table 2.

* Numbers in brackets represent percentages of single-grain ages in each sample. Dividing the percentages by 10 and then rounding them to their nearest integer derive the weights of individual Peak Ages (0 to 10) as discussed in section 3.4.2 (e.g., 10% would derive a weight of 1).

Depositional ages of the DH section were determined by correlating the DH section with the adjacent magnetostratigraphically dated KH and SB sections from Li et al. (2022).

† See Table 2 for the draining terranes of the modern river sand samples.

‡ See Supplementary Text S4 for further discussion.

Table 4. Vitrinite reflectance (%Ro) data of shales from the Cretaceous strata in the KH section.

Sample ID	Stratigraphic height (m)*	Approximate age (Ma) [#]	Number of analysis	Ro (%)	S.D.	Temp. (°C) ¹	Temp. (°C) ²
KRJ16-B-48	972	90±2	50	0.50	0.13	70	90
KRJ16-B-49	965	90±2	39	0.44	0.13	54	80
KRJ-16-B-31	568	97±2	51	0.67	0.17	106	114
KRJ-16-B-P48	360	100±2	34	0.61	0.13	94	107

Note: S.D. Standard deviation; Temp. Temperature.

* See Figure 2 for stratigraphic heights.

[#] Approximate ages are derived from Kaya et al. (2020).

¹ Temperature estimated from Barker and Goldstein (1990): $T(^{\circ}\text{C}) = (\ln(\%Ro) + 1.26)/0.00811$.

² Temperature estimated from Sweeney and Burnham (1990): $T(^{\circ}\text{C}) = 82.529 * \ln(\%Ro) + 147.51$.

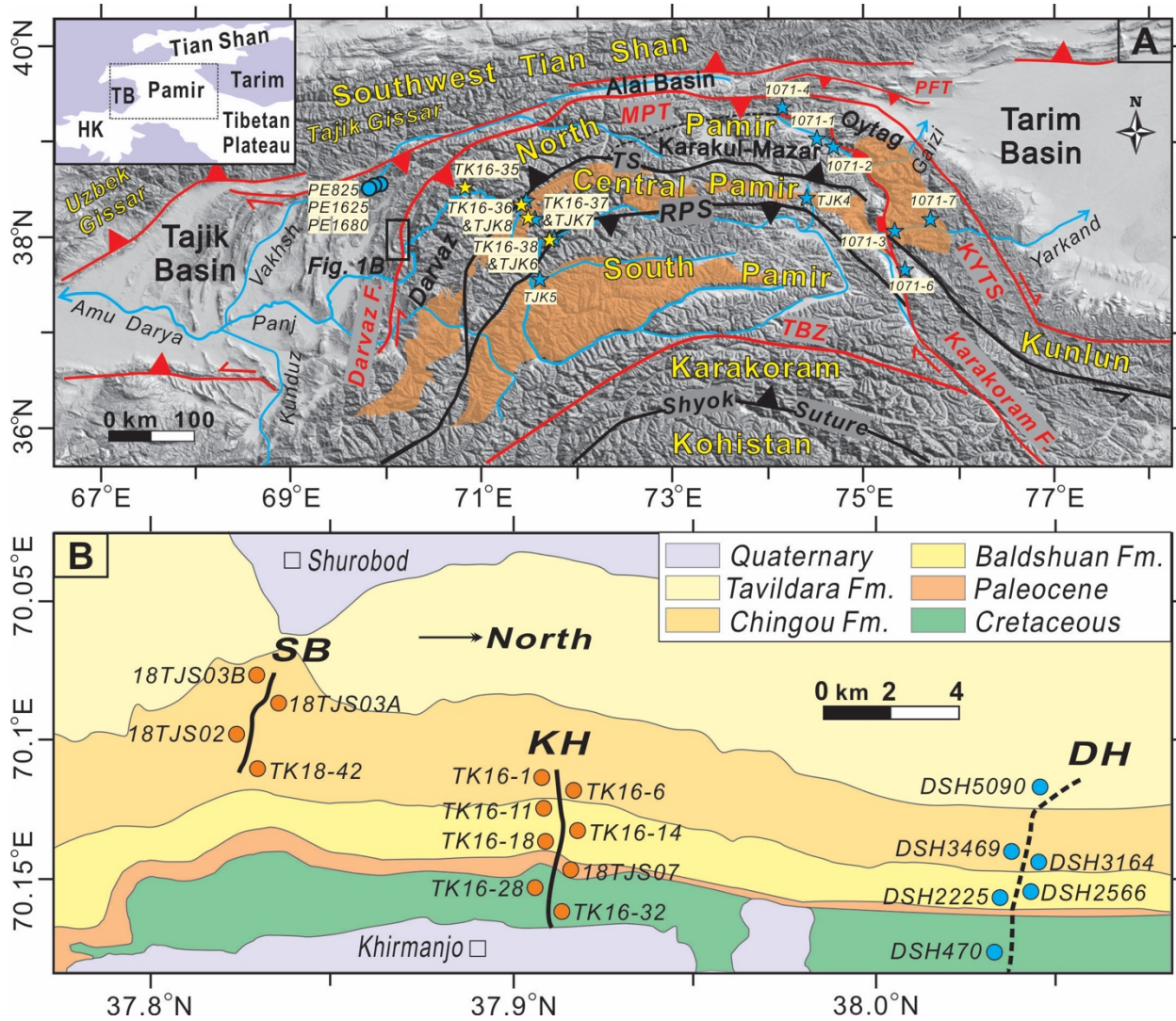
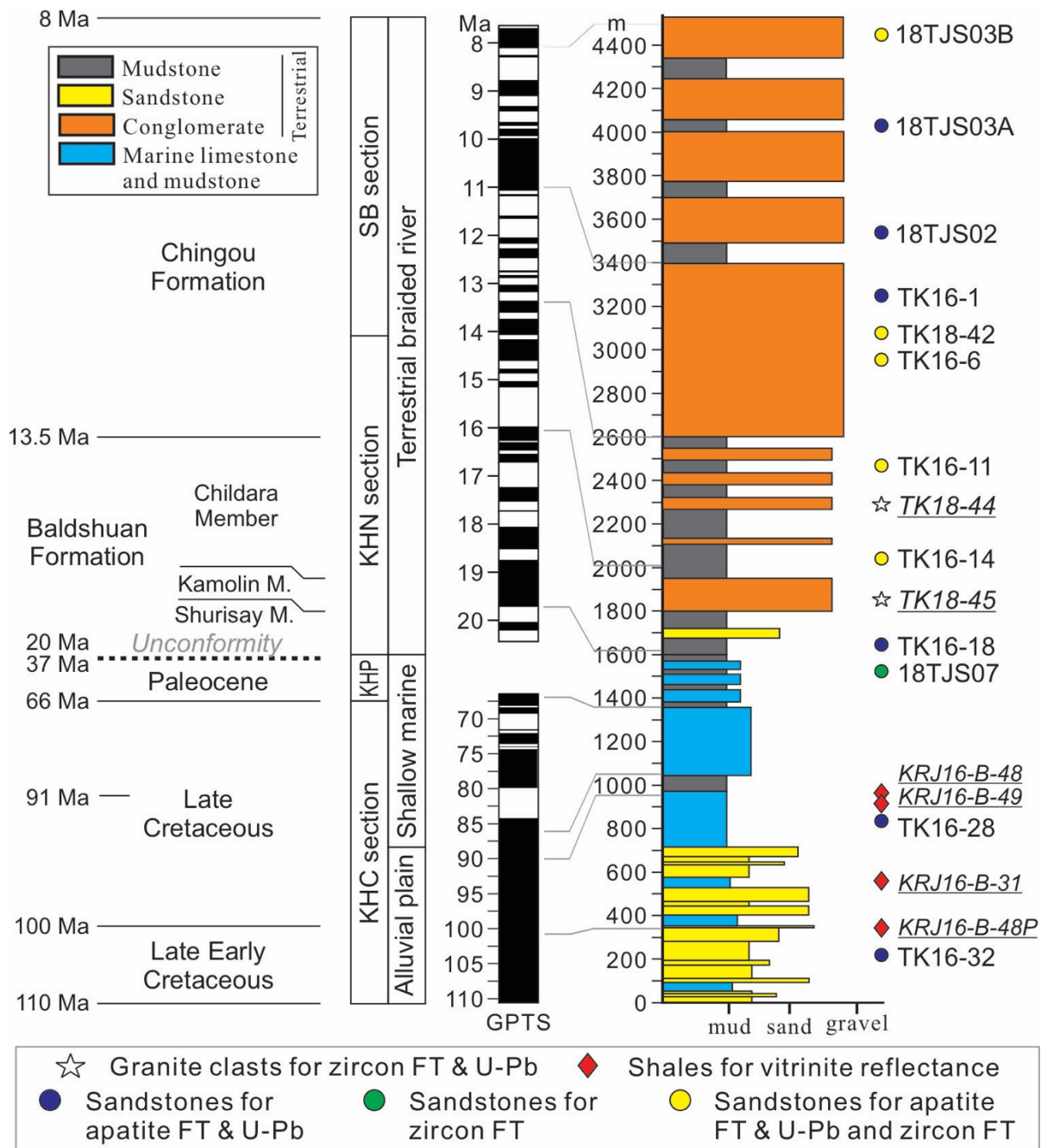


Figure 1

938

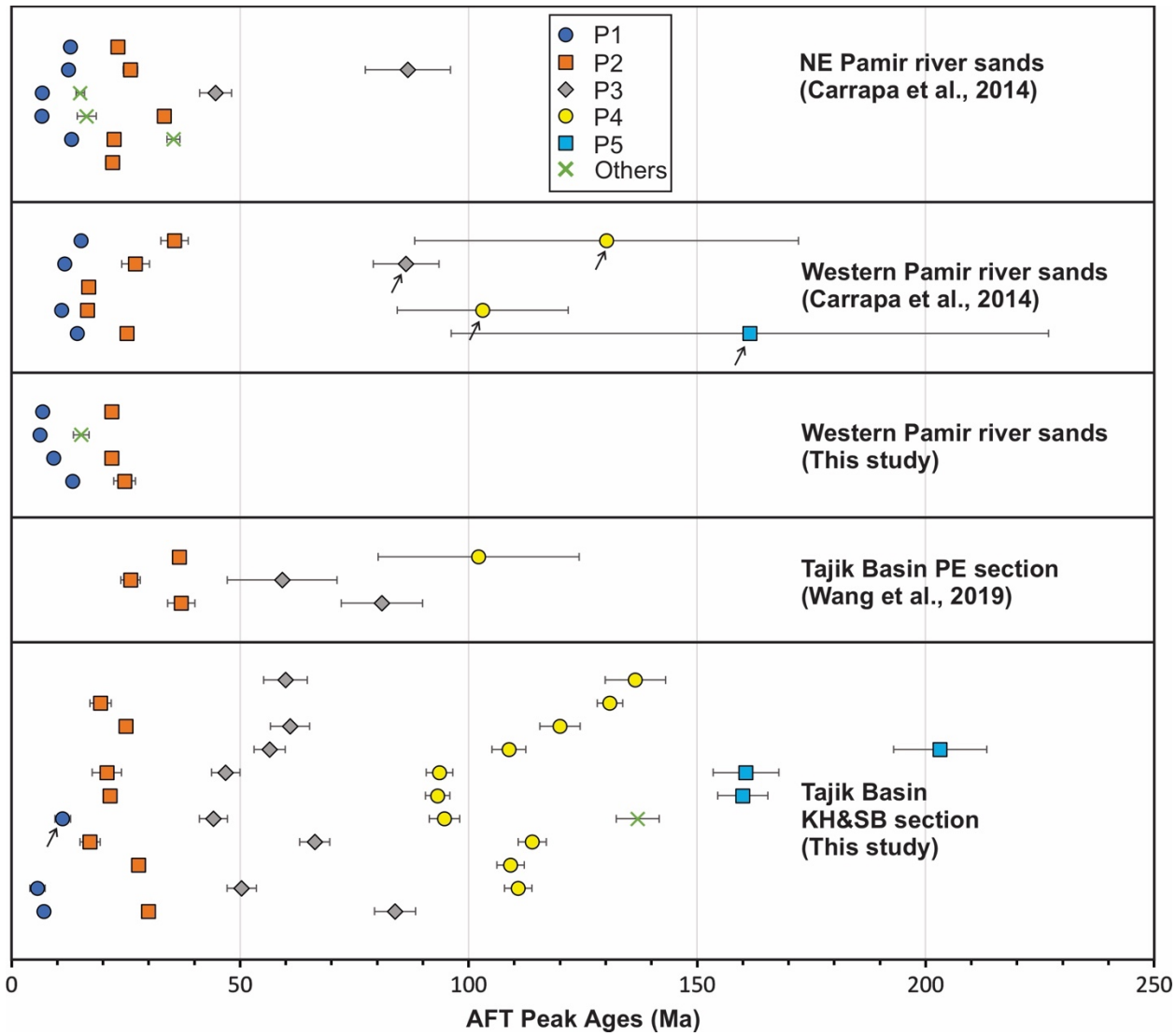
939



940

941

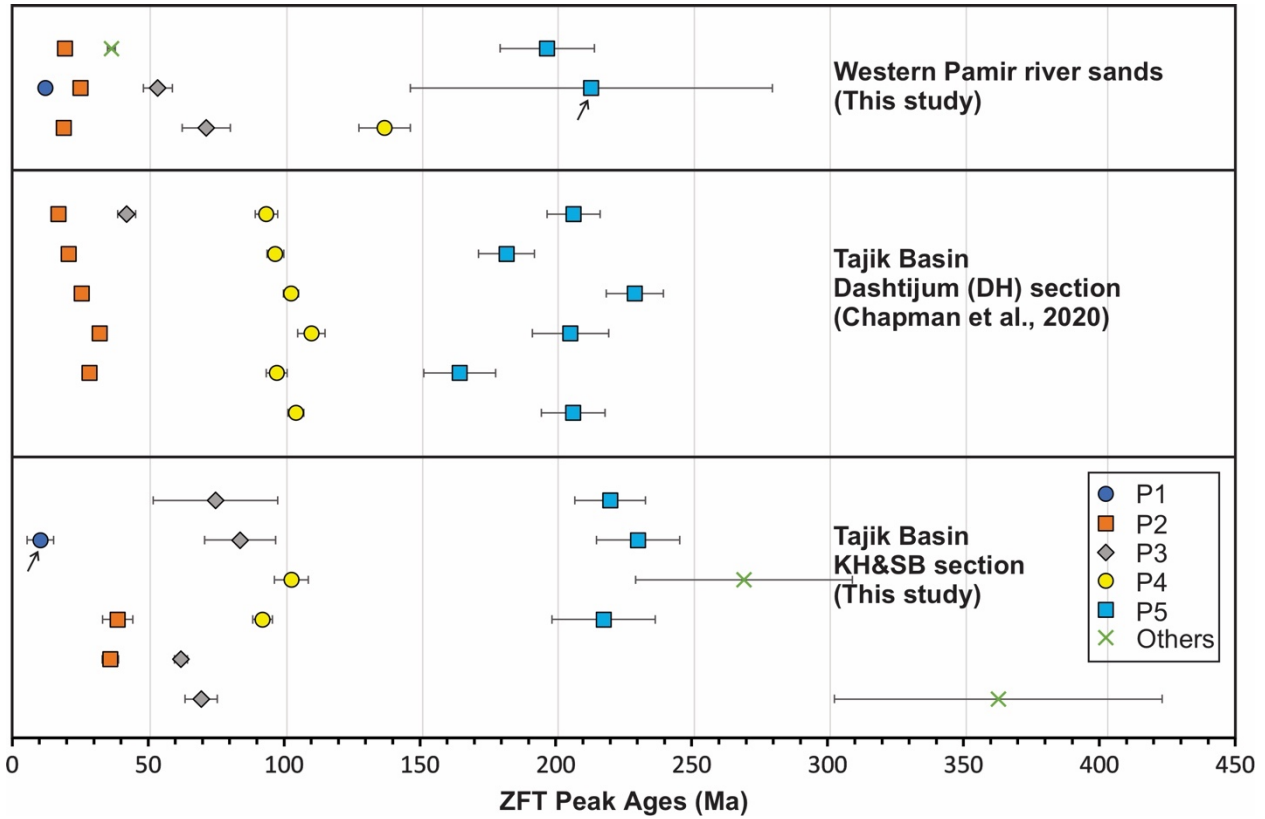
Figure 2



942

943

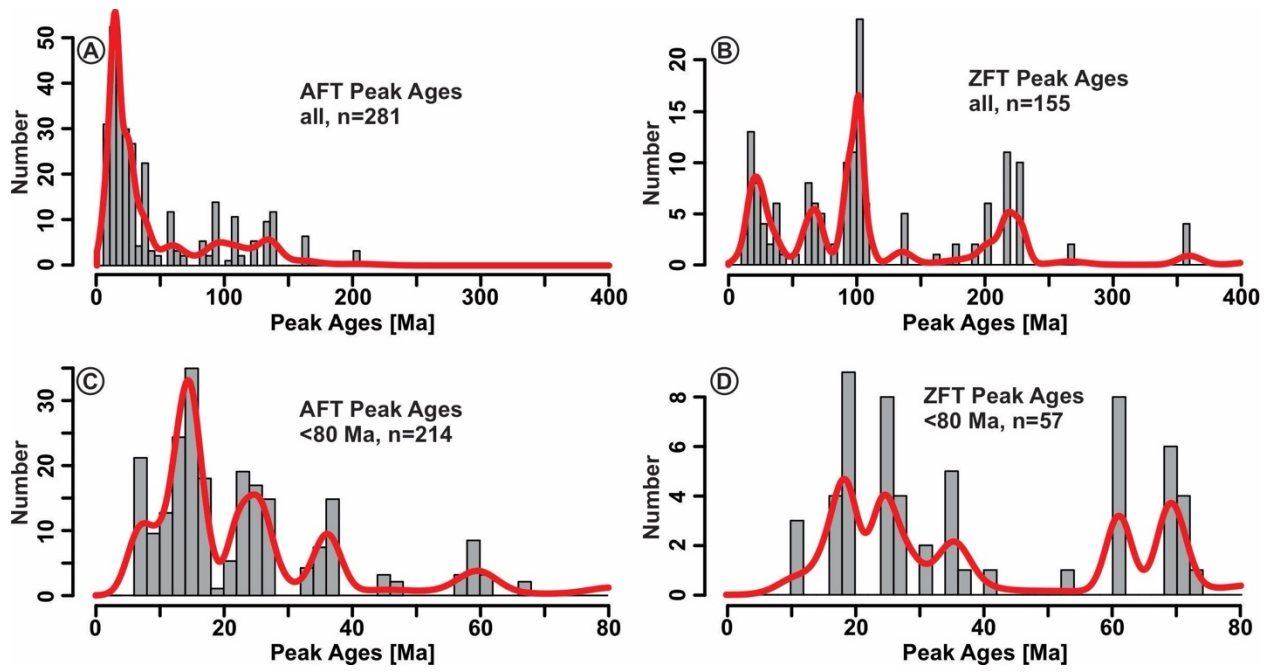
Figure 3



944

945

Figure 4

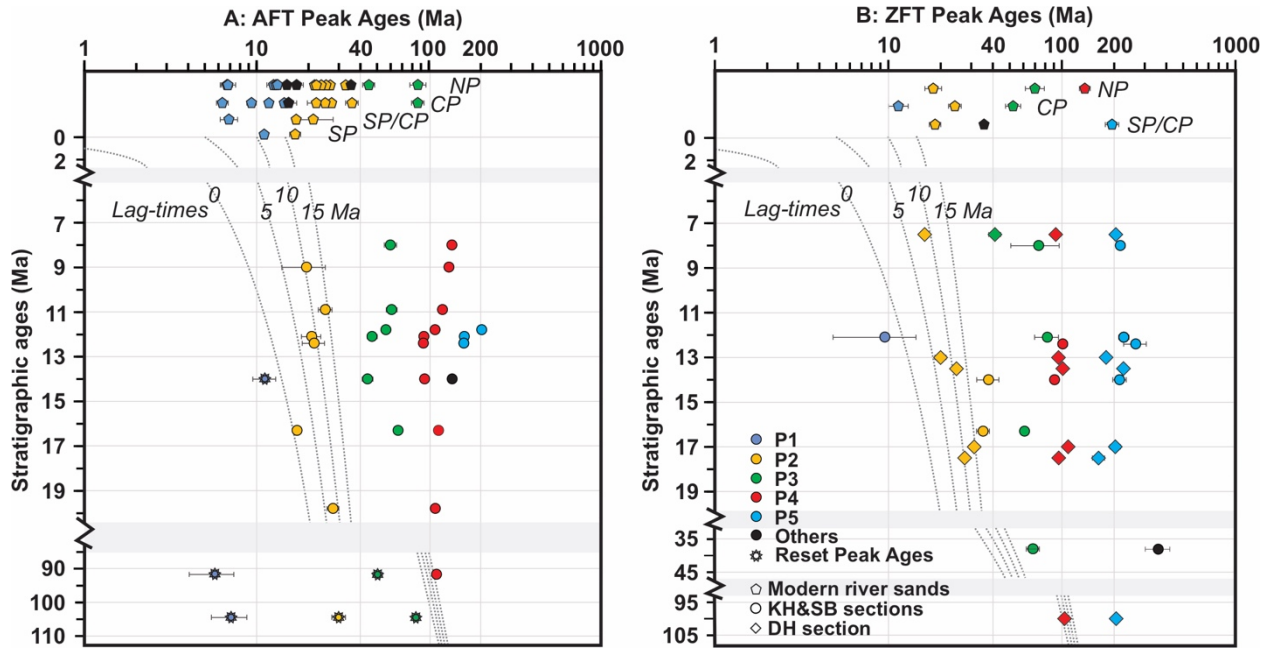


946

947

Figure 5

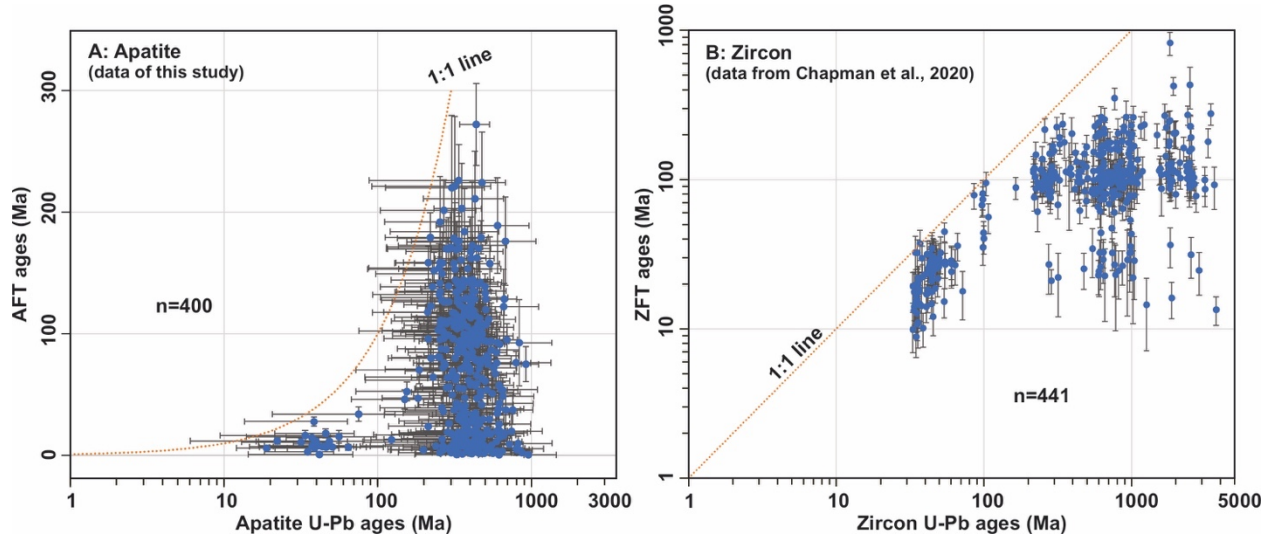
948



949

950

Figure 6



951

952

Figure 7